

Neutral-strange-particle production by 300-GeV protons

P. Skubic,* O. E. Overseth, and K. Heller

Physics Department, University of Michigan, Ann Arbor, Michigan 48109

M. Sheaff, L. Pondrom, P. Martin,† R. March,

R. Handler, and G. Bunce‡

Physics Department, University of Wisconsin, Madison, Wisconsin 53706

P. Yamin,‡ L. Schachinger, J. Norem,§ R. T. Edwards,¶

B. Edelman,|| and T. Devlin

Physics Department, Rutgers—The State University, Piscataway, New Jersey 08854

(Received 17 April 1978)

A neutral beam designed to transmit a high flux of Λ^0 hyperons with momenta above 50 GeV/c has been built and operated at Fermilab. Inclusive production cross sections per target nucleus have been measured for $p+A \rightarrow \Lambda^0 + X$, $p+A \rightarrow K_S^0 + X$, and $p+A \rightarrow \bar{\Lambda}^0 + X$ with 300-GeV protons incident on solid targets A = beryllium, copper, and lead. The region of phase space covered is predominantly projectile fragmentation: $0.2 \leq x \leq 1$, $0 \leq p_{\perp} \leq 2$ GeV/c. The A dependence of the inclusive cross sections is analyzed. The cross sections are compared to other work in pp collisions by extrapolating the A dependence to $A=1$. The results of measurements of Λ^0 and $\bar{\Lambda}^0$ polarization from the beryllium target are presented.

I. INTRODUCTION

This paper presents in one place the final results of the analysis of the operational characteristics of the Fermilab neutral-hyperon beam when produced by 300-GeV protons incident on various solid metal targets. The construction of a short neutral beam of this type was envisaged in the early planning stages of the then 200-GeV NAL accelerator.¹ Similar beams have been operated successfully at 24 GeV at CERN, and at 33 GeV at Brookhaven, predominantly for the study of the decay of the K_S^0 - K_L^0 complex,^{2,3} but also for the measurement of Λp total cross sections,⁴ and the Σ^0 lifetime.⁵ The particle mean decay path increases linearly with laboratory momentum, but the distance necessary to collimate the neutral beam and afford hadronic shielding between the production target and the detection apparatus grows much more slowly—essentially logarithmically. Thus it was recognized that if the yield of strange particles produced by protons remained about 10% of the total cross section as the bombarding energy increased, then the fluxes of particles with lifetime in the 10^{-10} -sec range available after collimation should increase substantially relative to neutrons and γ rays. The resulting higher fluxes of Λ^0 , $\bar{\Lambda}^0$, Ξ^0 , and K_S^0 offered the opportunity to study their production spectra and their interaction with ordinary matter in a beam line in much the same way as has been traditional for the more stable strange and ordinary mesons and baryons.

This paper is restricted to the properties of the production spectra of Λ^0 , $\bar{\Lambda}^0$, K_S^0 , the dependence

of these spectra on the atomic weight of the target nucleus, and the polarization of the Λ^0 and $\bar{\Lambda}^0$. The production and decay characteristics of the Ξ^0 hyperon and the study of the interactions of all these particles in hydrogen and deuterium will be treated in separate articles. Previous publications have covered some aspects of this work. An early version of the inclusive yields of Λ^0 and $\bar{\Lambda}^0$ and of the Λ^0 polarization has been reported.⁶ The Λ^0 polarization has been discussed in more detail.⁷ The spectra of Λ^0 , $\bar{\Lambda}^0$, and K_S^0 have been analyzed from the triple-Regge point of view.⁸ The A dependence of the Λ^0 spectra has been described in terms of a simple collision model.⁹ The present work supersedes all previous versions of the data, and emphasizes the general characteristics of the results rather than considering their compatibility with particular models. In the interest of completeness some of the results reported earlier are duplicated here.

It is traditional to measure the fluxes of produced particles in a new secondary beam and a new energy region early in the experimental program. Aside from their practical importance, these measurements can be of theoretical interest in understanding high-energy hadronic processes.^{10,11} The inclusive invariant cross section for a process $a+b \rightarrow c+X$, $E_c d^3\sigma/dp_c^3$, can be a function of the square of the total energy available $s_{ab} = (E_a + E_b)^2 - (\vec{p}_a + \vec{p}_b)^2$ and the momentum vector \vec{p}_c . Thus

$$E_c \frac{d^3\sigma}{dp_c^3} = f(s_{ab}, \vec{p}_c). \quad (1)$$

When divided by the absorption cross section σ_{ab} (the total cross section minus elastic scattering),

the resulting density function $\rho(s_{ab}, \vec{p}_c)$ integrated over all phase space gives the multiplicity of particle c

$$\langle n_c \rangle = \int \frac{d^3 p_c}{E_c} \rho(s_{ab}, \vec{p}_c), \quad (2)$$

$$\rho(s_{ab}, p_c) = \frac{1}{\sigma_{ab}} E_c \frac{d^3 \sigma}{d p_c^3}. \quad (3)$$

The most commonly produced particles are pions. It is experimentally known that σ_{ab} and $\langle n_\pi \rangle$ increase very slowly with increasing s_{ab} at sufficiently high s . It is also known that the dependence of ρ on the vector \vec{p}_c is different for longitudinal and transverse components. Thus at large s the functional dependence of ρ on the transverse momentum $\vec{p}_{\perp c}$ becomes approximately s independent. The increasing energy available thus goes neither into multiplicity nor transverse momentum—leaving the longitudinal momentum component $p_{c\parallel}$ as the only other candidate. A conjecture consistent with this behavior is Feynman scaling,¹² which states that if $p_{c\parallel}$ in the (a, b) center of mass is divided by its maximum value to give a dimensionless quantity $x = p_{c\parallel}/p_{\parallel \max} \approx 2p_{c\parallel}/\sqrt{s_{ab}}$ then the explicit s dependence of Eq. (1) goes away at large s , i.e.

$$E_c \frac{d^3 \sigma}{d p_c^3} \xrightarrow{\text{large } s} f(\vec{p}_{c\perp}, x_c). \quad (4)$$

Invariant cross sections for $a + b \rightarrow c + X$ in terms of the variables $(\vec{p}_{c\perp}, x_c)$ become energy independent according to this hypothesis.

A distinction is made between two kinematic regions for particle c . If x_c is near ± 1 , then the particle is thought to be associated with the fragmentation of the projectile or the target. If on the other hand $x_c \sim 0$, the particle is said to come from the central region. There is of course a smooth transition between the two regions. Equation (4) is thought to hold in both regions, but the mechanisms responsible for its validity could be different. Features common to both particles (a, c) such as charge, or strangeness, or baryon number, tend to enhance the cross section as $x_c \rightarrow \pm 1$ over that observed when such features are not common. This enhancement phenomenon is called the leading particle effect. Quantum numbers of the initial-state particles presumably play a less important role in the central region, where baryons, for example, are produced predominantly in pairs.

Experimental data serve to test these ideas. Is Eq. (4) valid at accessible energies for various combinations of particles (a, b, c) , and in all of phase space for particle c ? In what manner as a function of s is this limiting form approached? What is the shape of the distribution function in

the central region? In the region as $x \rightarrow 1$? Reference 10 gives a general survey of the subject, and Ref. 11 gives a review of pp data at several energies. Bubble-chamber results have been collected and summarized by Whitmore.¹³ The most extensive data set is for $(a, b) = (p, p)$, which has been extended to energies $\sqrt{s} \sim 60$ GeV by experiments at the CERN ISR. The most commonly observed final-state particles c are π^\pm , K^\pm , p , and \bar{p} , although charged^{-14,15} and neutral^{-16,17} hyperon yields have also been measured. Fragmentary data exist for complex nuclear targets.¹⁸ It is impossible to do justice to this wealth of information in a few sentences, but the picture very roughly is as follows. Equation (4) seems essentially satisfied in $p + p \rightarrow c + X$ at $\sqrt{s} = 7$ GeV for $c = \pi^\pm$, K^\pm , and p , but not for K^- and \bar{p} . An incident proton leads to enhanced flux of Ξ^- and Λ^0 hyperons relative to mesons as $x \rightarrow 1$, a leading particle effect which is not so apparent for Ξ^- . Very little data exist in the literature on the yields of anti-hyperons.

The present paper gives invariant cross sections $E d^3 \sigma / d p^3$ for $(p + A \rightarrow c + X)$ with target nuclei beryllium, copper, and lead and with final-state particles $c = \Lambda^0$, K_s^0 , and Λ^0 . No distinction was made between directly produced Λ^0 's and daughters from Σ^0 decay. The region of phase space covered by these measurements is predominantly projectile fragmentation with $0.2 \leq x \leq 1$ and $0 \leq p_\perp \leq 2$ GeV/c. This is shown on a Peyrou plot in Fig. 1. The data were taken at fixed

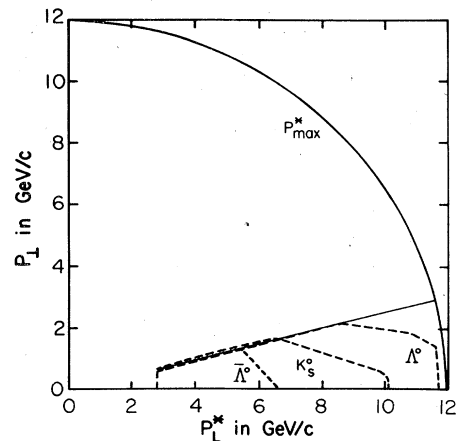


FIG. 1. Plot of transverse momentum versus longitudinal momentum in the nucleon-nucleon center of mass. The radius of the circle is $p_{\max}^* = \sqrt{s}/2 = 11.9$ GeV/c. Data were taken at fixed laboratory angles—equivalent to fixed angles on this plot, from $p_\perp = 0$ out to where the solid line intersects the circle at $p_\perp = 2.7$ GeV/c. The dotted lines represent the effective cut offs in the respective spectrum measurements where, because of the kinematic dependence of the cross sections, the yields of data go to zero.

laboratory angles between 0 and 9 mrad. In the text that follows, the experimental arrangement is described in some detail; data reduction and statistical and systematic errors are discussed; the dependence on atomic weight is expressed as a power of A ; empirical fits to the inclusive spectra are obtained to facilitate interpolation between the fixed angle points; comparison is made to other experiments on hydrogen by extrapolation to $A = 1$; and the kinematic dependence of the Λ^0 polarization as well as measurements of the $\bar{\Lambda}^0$ polarization are presented.

II. EXPERIMENTAL APPARATUS

A. Proton beam

Figure 2 shows an elevation view of the apparatus. The 300-GeV diffracted proton beam in the Meson Laboratory M-2 line at Fermilab was directed onto solid targets located at T . The 6-mm diameter targets were mounted in chambers in a styrofoam revolver cylinder which could be rotated remotely. The target thicknesses were: Be, 28.3 g/cm²; Cu, 41.6 g/cm²; Pb, 55.8 g/cm². One target chamber was empty to study production from spurious sources. Typically, 85 to 90% of the proton beam was contained within the 6 mm diameter. A scintillator telescope consisting of a 6-mm-diameter scintillator, a 12-mm-diameter scintillator, and a 5-cm-diameter scintillator with a 6-mm hole in its center (the halo) was used to count the proton beam at low intensity ($\sim 10^6$ per 800-msec spill), and to check the absolute calibration of the argon-filled ionization chamber IC. The gas path in the chamber was 4 cm at atmospheric pressure, and the resulting charge was integrated on 1100 pF to give a voltage read by an electrome-

ter. The average of 48 scintillator-calibration runs through the course of the experiment gave

$$k_{IC} = (0.070 \pm 0.003) \text{ volts per } 10^6 \text{ protons, } (5)$$

corresponding to 120 ion pairs collected per cm of gas per proton. At higher intensities the IC served as the primary monitor, although the halo counter was used to measure the fraction of the proton beam outside the 6-mm circle up to total fluxes of a few $\times 10^7$. The bending magnet $M1$ shown in Fig. 2 was used to vary the production angle viewed at the target by the fixed collimator. By displacing the beam vertically a few centimeters and restoring it to the production target with $M1$, angles relative to the collimator axis of up to 9 mrad were achieved. The excitation of $M1$ required to center the displayed beam on the target gave the primary measurement of production angle. Figure 3 shows a detail drawing of the proton beam monitors, the target, and the collimator mouth. The two beam multiwire proportional chambers served to check beam alignment on the target and gave auxiliary measurements of the proton production angle.

B. Neutral-beam collimator

The neutral beam was formed by a collimation system incorporating a defining aperture near the center of a channel 5.3 m long with a vertical magnetic field of 23 kG. The central aperture was a 4-mm-diameter hole in a tungsten plug 56 cm long. The collimator design is shown in detail in Fig. 4. The magnetic field bent the proton beam and charged particles produced at the target into the base of the tungsten plug, or into larger aperture brass collimators upstream of the

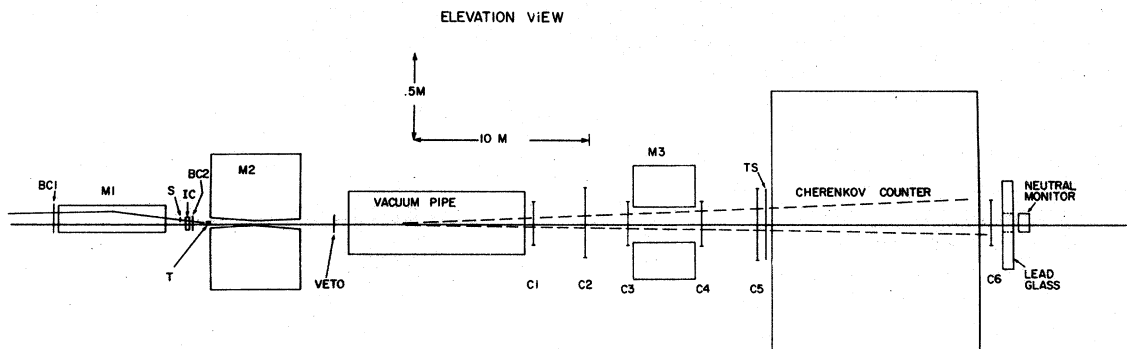


FIG. 2. Elevation view of the apparatus. A displaced incident proton beam at 300 GeV is shown deflected onto the production target at T at 9 mrad. $M1$ is the restoring magnet. $BC1$ and $BC2$ are proton beam profile monitors. S is a scintillator telescope, and IC is the argon-filled ionization chamber, the primary-beam monitor. The collimator magnet $M2$ swept charged particles out and defined the neutral beam. The decay volume began downstream of the veto scintillator. $C1$ through $C6$ are multiwire proportional chambers, and $M3$ is the analyzing magnet. The timing scintillator is labeled TS . The helium-filled threshold gas Cherenkov counter is followed by the lead-glass wall and the neutral-monitor telescope.

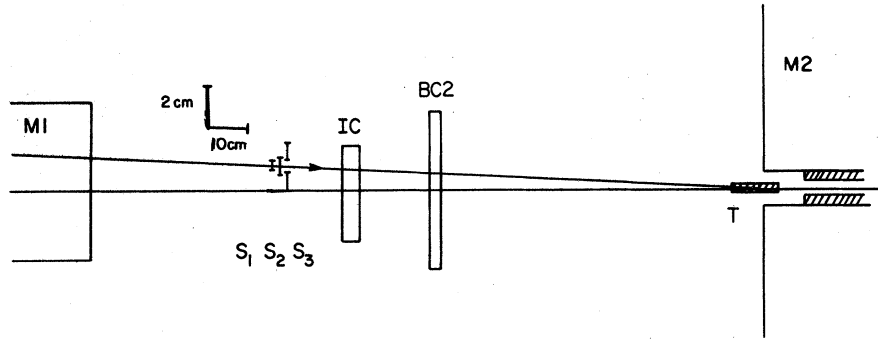


FIG. 3. Detail of the proton-beam monitors and the target region. The beam is shown incident at 9 mrad, and the monitor scintillators are appropriately displaced to be centered on the beam. The ion chamber was calibrated at low beam intensity using $(S_1 \cdot S_2) + S_3$ as a total flux monitor.

plug. Downstream of the plug gradually increasing apertures in brass collimators served to remove secondaries made in the defining hole. No attempt was made to remove γ rays or any other component of the neutral beam selectively by the insertion of absorber in the collimator channel. Charged particles were eliminated by this system. Secondary sources of neutrals made by the neutral beam itself had to be accounted for at low energies, a correction which will be discussed in Sec. III. The effective solid angle of the system was calculated to be

$$\Delta\Omega = (1.20 \pm 0.07) \times 10^{-6} \text{ sr.} \quad (6)$$

C. Spectrometer

A scintillator veto defined the beginning of the decay volume 1.75 m downstream of the 1.1-cm-diameter collimator output opening. Neutrals decayed in an evacuated pipe 11 m long. The first of six multiwire proportional chambers (MWPC's) was placed next to the output window of the decay vacuum. The three chambers upstream of the spectrometer magnet, labeled *M3* in Fig. 2, were separated from one another by 3-m long drift spaces. The active areas of these chambers were as follows: CH 1: 256 vertical wires \times 128 horizontal wires; CH 2: 128 \times 128 wires at 45°; CH 3: 256 vertical wires \times 128 horizontal wires. The wire spacing in each chamber was 2 mm. All chambers were operated in an atmosphere of 70% argon, 30% isobutane, and 0.3% freon bubbled through methylal at 4°C. Normal plateau operating voltage was 4.2 kV. Two methods were routinely used to check chamber efficiency. Periodically all magnets were turned off, the target was removed, and the direct proton beam at reduced intensity was brought through the spectrometer. By triggering the chamber read-out system on scintillators in the beam line, the geometrical

alignment and efficiency of the spectrometer could be measured. During normal running only one hit was required in any chamber to trigger the system (see Sec. II E below), but the majority of events had "V" topology, with two hits in each chamber, thus affording a technique to monitor efficiency continuously. Single-hit efficiency for each chamber varied between 97.5% and 99.5% during the course of the experiment.

The spectrometer magnet was a ferric superconductor with an aperture 60 cm (horizontal) \times 20 cm (vertical), an effective length of 190 cm, and a peak central field of 18 kG. Chamber 4 behind the spectrometer magnet had 316 (vertical) \times 128 (horizontal) wires and chamber 5, 3m downstream, had 640 (vertical) \times 192 (horizontal) wires. The drift spaces between each of the five upstream chambers, including the magnet gap *M3*, were filled with polyethylene bags of atmospheric helium gas

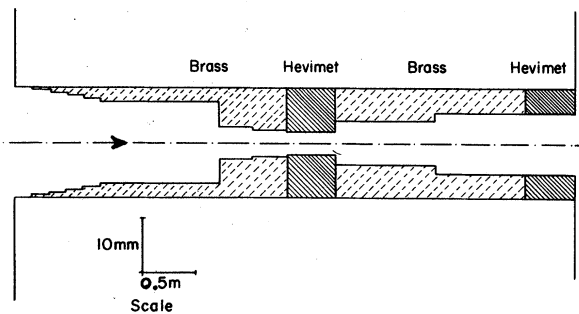


FIG. 4. Design of the neutral-beam collimator. The 300-GeV proton beam incident from the left was deflected into the brass step upstream of the defining aperture. Collimation on the downstream side served to screen secondary sources from the surfaces of the defining slit. The magnetic field integral along the collimator was 117 kGm.

to decrease interactions and multiple scattering. A scintillator 0.3 g/cm^2 thick was placed behind chamber 5 to give a sharp timing signal for the electronics. A low-pressure threshold gas Cherenkov counter 11-m-long separated chambers 5 and 6. This counter was normally filled with helium at 250 torr, corresponding to a proton threshold momentum of $170 \text{ GeV}/c$, and served to discriminate between baryons and mesons below this momentum which went through the counter near its axis. Its very simple optical system consisted of a tilted 1-m focal-length Lucite mirror, a quartz window, and a quartz face 5-cm-diameter phototube with high photocathode conversion efficiency. The total amount of material in the neutral beam was kept low. Each chamber presented about 25 mg/cm^2 of carbon equivalent to the beam. The total material from the downstream edge of 0.7-cm-thick veto scintillator through chamber 5 was about 0.6 g/cm^2 . The mirror and back Al window in the Cherenkov counter added another 1.7 g/cm^2 just before chamber 6. The spectrometer magnet was usually operated at 70% full field at 300 GeV, so that charged particles with momenta above $\sim 50 \text{ GeV}/c$ struck the active area of chamber 6, which had 316 (vertical) $\times 128$ (horizontal) wires. The different sizes chosen for chambers 5 and 6 can be understood from the asymmetry inherent in the decay $\Lambda^0 \rightarrow p\pi^-$ caused by its very low Q value. If the Q value were zero the π and p would have the velocity of the Λ^0 , and consequently a momentum ratio $p_\pi/p_p = m_\pi/m_p$. Thus chamber 5 can be thought of as the pion detector, and chamber 6 the proton detector.

D. Lead-glass and neutral monitor

A lead-glass wall large enough to intercept γ rays originating in the decay region and transmitted through the aperture of $M3$ was placed behind chamber 6. 72 blocks were arranged vertically in five rows in a staggered array, three rows 15 blocks long and two rows 14 blocks long, with the center block in the neutral beam removed. Each block was $100 \text{ mm} \times 100 \text{ mm} \times 384 \text{ mm}$ ($12X_{\text{rad}}$). The array could be moved normal to the neutral beam for calibration, which was done with electron pairs made in the beam line. Pulse height from each block was recorded for every event. Since the purpose of the array was to detect γ rays from the decay chain $\Xi^0 \rightarrow \Lambda^0 \pi^0$, $\Lambda^0 \rightarrow p\pi^-$, $\pi^0 \rightarrow \gamma\gamma$, and the Ξ^0 results are not discussed in this paper, further details regarding the behavior of the lead glass will be deferred.

Behind the lead-glass wall, 40 m from the output face of the collimator, the neutral beam was approximately 10 cm in diameter. A secondary-

beam-intensity monitor, shown in detail in Fig. 5, was placed at this location to serve as a check on the stability of the primary monitors at fixed production angle, and to give a measure of the total flux of neutrals in the beam. The monitor telescope contained a veto scintillator and components to identify selectively the γ rays and neutrons in the beam.

E. Trigger electronics

Proportional wires in the chamber planes could be used as their own trigger counters. The vertical wires (horizontal coordinates) could be combined to form hodoscope elements in strips 64 wires wide (128 mm), although a mesh this fine was not usually used in the trigger. The signals from the horizontal wires were all added together in an OR circuit and placed in coincidence with the vertical wire pattern to give a chamber output pulse. This logic was done at the chamber and coincidences between chambers were formed in the electronics room. In this way, scintillators, MWPC patterns, and the Cherenkov signal could all be mixed together in any desired way to generate the good event trigger. A very unrestricted trigger—at least one hit in each of the first five chambers—was used for the yield measurements reported here.

The trigger logic is shown very schematically in Fig. 6. An earlier version of the read-out system has been previously described.¹⁹ The coincidence logic sent an enable pulse to each chamber, which allowed flip-flops to be set, thus storing the coordinate information pertinent to that event. It also generated its own dead time, which remained in force until the read-out process was completed, and sent a priority interrupt to the PDP 11/45 computer. The computer read all the

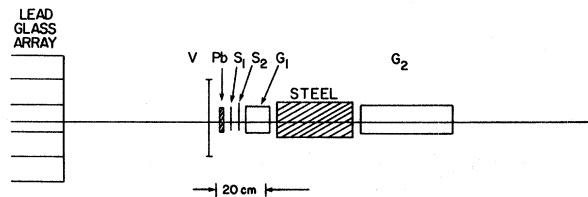


FIG. 5. Elevation view of the downstream monitor used to count the neutron and γ -ray components of the neutral beam. This figure has the same horizontal and vertical scales. The beam passed through a hole in the center of the lead-glass wall, where a block was removed. Lead-glass block G_1 is $3X_{\text{rad}}$ thick, and G_2 is $12X_{\text{rad}}$ thick, while there are three interaction lengths of steel between G_1 and G_2 . For monitor purposes a γ ray was defined by $\gamma = \bar{V} \cdot S_1 \cdot S_2$, and a neutron by $n = \bar{C}_1 \cdot G_2$.

data in single word transfers via CAMAC dataways, including latch and pulse-height information where appropriate, and all of the chamber wire hit addresses, up to a maximum of 63. The chamber data appeared in sequence on a register at a single crate address in CAMAC. The typical time to read a complete event was 500 μ sec. The act of reading reset all the registers, and the dead time was removed by the computer when the next event could be accepted. The ion chamber was not gated, so a dead-time correction had to be made to its reading to obtain the usable beam flux. Once each accelerator cycle, at the end of the beam spill, a separate CAMAC crate containing various gated and ungated monitor scalars and the accumulated charge from the ion chamber for that pulse was read and cleared by the computer, thus recording the necessary normalization information.

F. On-line program

A monitor program was written for the PDP 11/45 which read the data for each event from CAMAC, stored it in a buffer in core memory, and wrote events directly on magnetic tape when the buffer was full. Tape writing during the spill limited the event rate to 220 events/spill. (This rate has been subsequently increased to 660 events/spill by writing on a disk.) The events remaining in the buffer at the end of the spill were transferred to histogram storage on the disk, where the hit patterns received from each chamber plane were stored to furnish an on-line check on the quality of the chamber operation. Latch patterns and pulse-height distributions from various counters were also histogrammed. The scaler and IC data read at the end of each spill were accumulated in the computer and written to magnetic tape in a special scaler record every eight spills.

III. DATA REDUCTION

A. Reconstruction

A normal data tape contained 80 000 triggers and required 45 minutes of running at an intensity sufficient to saturate the rate capability of the apparatus. The incident proton beam intensity was varied between about 2×10^6 protons/pulse at 0 mrad to 10^7 protons/pulse at 9 mrad to maintain the trigger rate. No calculations were performed by the on-line program to reduce the data written onto tape. A pattern-recognition program was used off line to search for events which had the neutral "V" topology characteristic of the decays $\Lambda^0 \rightarrow p\pi^-$, $\Lambda^0 \rightarrow \bar{p}\pi^+$, and $K_S^0 \rightarrow \pi^+\pi^-$. The momentum

components of each track and the vertex coordinates were then written on a compacted tape. The fraction of original triggers retained on the compacted tape varied from about 50% at the smaller angles to about 25% at 9 mrad. The events not fitting a "V" topology were γ -ray conversions in the small amount of material in the decay region—which had an apparent "Y" topology—multi-track events from neutron interactions, and occasional single tracks. About 1% of the real "V" events were lost because of extra accidental tracks, and a correction was made for this loss in calculating the cross sections.

The invariant mass of the "V" was then calculated from the measured momenta of the positive and negative particles. The exact formula was used in the computation

$$M_{+-} = [m_+^2 + m_-^2 + 2E_+E_- - 2\vec{p}_+ \cdot \vec{p}_-]^{1/2}, \quad (7)$$

but for many purposes the high-energy, small-

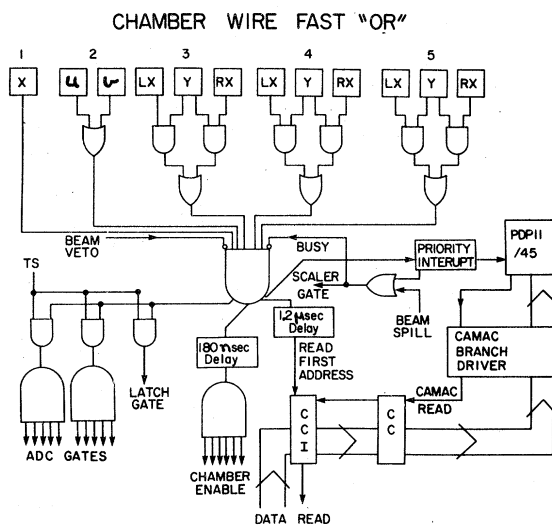


FIG. 6. Simplified diagram of the electronic logic. Signals from the planes in chambers 1 through 5 were combined as shown to require at least one charged particle. This coincidence was mixed with the beam veto and the busy gate to generate a signal which was sent back to the chambers to enable the wire addresses to be latched. This signal delayed by 1.2 μ sec initiated the reading and storage of the first hit wire address in the CCI (chamber-CAMAC interface). A priority interrupt was also sent to the PDP 11/45 Computer, which initiated a direct memory access read through the CAMAC branch driver and the CC (crate controller). The fast chamber coincidence, mixed with the timing scintillator (TS) was also used to gate the lead-glass signals into the analog-to-digital converters, and to set the pattern latches.

angle approximation is quite accurate

$$M_{+-} = \left[m_+^2 \left(1 + \frac{p_-}{p_+} \right) + m_-^2 \left(1 + \frac{p_+}{p_-} \right) + p_+ p_- \theta^2 \right]^{1/2}. \quad (8)$$

The following mass hypotheses were assumed for (m_+, m_-) : (m_p, m_π) , (m_n, m_p) , and (m_n, m_π) for Λ^0 , $\bar{\Lambda}^0$, and K_S^0 , respectively. The window for acceptance for a particular mass hypothesis was defined by $\Delta m \leq 3\sigma$, where $\Delta m = |\text{calculated mass} - \text{true mass}|$, and $\sigma = \text{standard-deviation error in the mass calculation}$, a quantity derived from the errors in spatial reconstruction for each event. It was possible for particular events to satisfy both the Λ^0 and K_S^0 , or $\bar{\Lambda}^0$ and K_S^0 masses simultaneously. The Λ , K ambiguity occurs via Eq. (8) when $(1 + p_-/p_+) = (m_\Lambda^2 - m_K^2)/(m_p^2 - m_\pi^2)$, which corresponds to a real angle in both the Λ^0 and K_S^0 center-of-mass at these energies. The threshold gas Cherenkov counter could resolve this ambiguity for protons (or antiprotons) with momenta below 170 GeV/c, but it was found less complicated in measuring the cross sections to make firm assignments of particle identity, and to correct later for misidentification with the help of the Monte Carlo program to be described below.

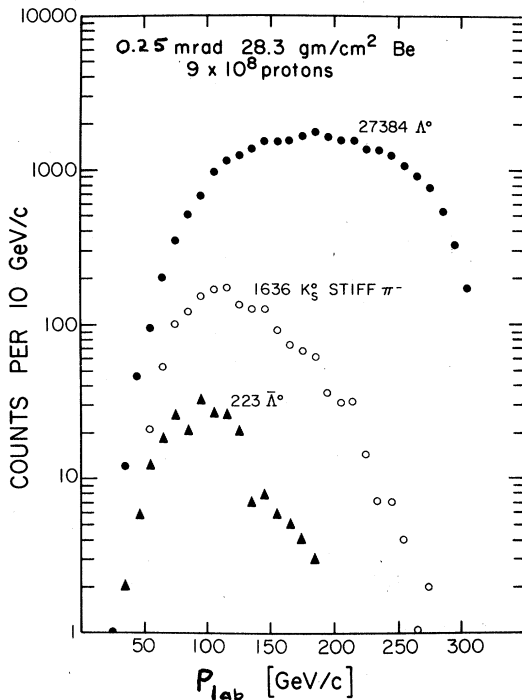


FIG. 7. Spectrometer data for a typical 0.25-mrad tape after being subjected to all of the selection criteria and cuts discussed in the text, but not corrected for detection efficiency. The yields in the momentum bin centered at 145 GeV/c on this plot are carried through all the calculations necessary to obtain invariant cross sections in the Appendix.

Thus if $p_+ > p_-$ and $M_{p\pi} \approx M_\Lambda$ [full width at half maximum (FWHM) = 6 MeV/c²], the event was called a Λ^0 regardless of whether it simultaneously satisfied the K hypothesis or not. Events with $p_+ > p_-$ and $M_{\pi\pi} \approx M_K$ (FWHM = 15 MeV/c²) $M_{p\pi} \neq M_\Lambda$ were contaminated with a background of poorly fit Λ^0 's. This effect was particularly troublesome at small production angles, where at high momenta the Λ/K ratio exceeded 100 (see Fig. 7). To be consistent, none of these events were used in the K_S^0 analysis. Events with $p_- > p_+$ and both $M_{\pi\bar{p}} \approx M_{\bar{\Lambda}}$, $M_{\pi\pi} \approx M_K$ (1.5% of the K 's) were rejected. The K_S^0 data sample came from events with $p_- > p_+$, $M_{\pi\pi} \approx M_K$, $M_{\pi\bar{p}} \neq M_{\bar{\Lambda}}$; and the $\bar{\Lambda}^0$ data sample from events with $p_- > p_+$, $M_{\pi\bar{p}} \approx M_{\bar{\Lambda}}$, $M_{\pi\pi} \neq M_K$. Six percent of the "V" events did not fall within any mass window. Most had vertices at the vacuum windows, and were produced by neutrons. A small correction was made for lost strange particles. At 0 mrad the "V" event sample after sorting by these mass hypotheses became 94% Λ^0 's, 5% K_S^0 , and 1% $\bar{\Lambda}^0$.

The event yields as a function of angle including the neutron and γ -ray monitor yields are displayed in Fig. 8. Table I shows the number of events for each particle hypothesis for the various angles and

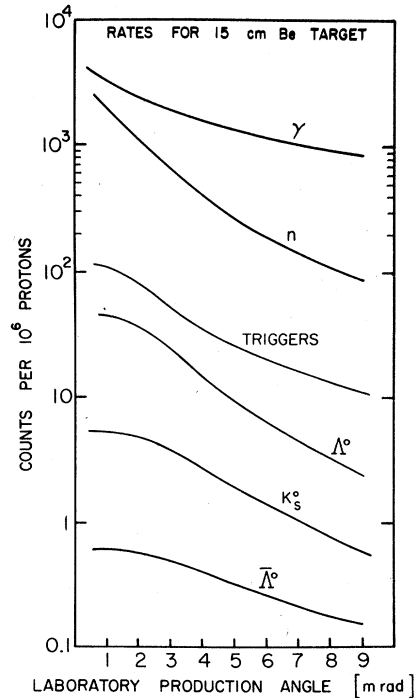


FIG. 8. Rates as a function of angle for the 15-cm-long beryllium target. " γ " and " n " are defined in the caption to Fig. 5. The other curves refer to the spectrometer, and show the yields of triggers Λ^0 , K_S^0 , and $\bar{\Lambda}^0$, respectively. The contribution of γ -ray conversions to the trigger rate increased with increasing production angle.

TABLE I. Number of Events

Production Angle (mrad)	Λ^0			$\bar{\Lambda}^0$			K_S^0		
	Be	Cu	Pb	Be	Cu	Pb	Be	Cu	Pb
0.25	149 000	76 200	54 200	1 072	654	561	8 850	4 910	3 620
0.9	114 000	53 700	28 900	900	555	319	7 480	3 790	2 050
1.5	84 200	30 900	30 000	748	354	371	5 770	2 260	2 340
2.9	78 600	...	26 100	1 100	...	447	6 940	...	2 690
5.0	86 300	...	19 300	2 230	...	577	10 700	...	2 440
6.9	46 000	...	15 700	1 920	...	698	7 010	...	2 360
8.8	35 500	8 620	12 400	1 980	508	736	5 750	1 360	2 050
Total	593 600	169 420	186 600	9 950	2 071	3 709	52 500	12 320	17 550

production targets. Figure 7 shows the observed momentum spectra at 0.25 mrad from one magnetic tape.

B. Cuts

The event sample was subjected to fiducial cuts in addition to the mass window to insure that the events were well within the apertures of the system. Hits in chamber 1 had to be within 64 wires of the chamber center. For the other chambers, borders typically 8 to 16 wires wide were excluded around the edges of the active areas. The decay vertices were required to be within a 10-m path inside the vacuum tank. The total momentum vector of the parent neutral particle was extrapolated back to the plane of the target (about 10 m upstream), and the distance R between the extrapolated point and the target center was calculated. The precision of this extrapolation was determined by the spatial resolution of the spectrometer. Typically, 90% of the "V" events had $R^2 < 40 \text{ mm}^2$, compared to an acutal target $R^2 = 9 \text{ mm}^2$. A cut was made to eliminate events with $R^2 > 40 \text{ mm}^2$. These cuts combined rejected 25% of the original "V" sample.

C. The Monte Carlo program

A cornerstone of data analysis is an accurate Monte Carlo program which simulates the configuration of the experimental apparatus as faithfully as possible and allows accurate calculation of geometrical acceptance and the effects of various cuts. The present Monte Carlo program generated Λ^0 's and K_S^0 's at the target with the appropriate distribution in space, propagated them through the collimator with the correct lifetimes,^{20,21} allowed them to decay via the charged mode after the veto counter, and generated wire hits in the spectrometer. Tapes prepared in this

way were then analyzed by the pattern-recognition and other programs just like real data. Vertex and target pointing distributions, momentum spectra, invariant-mass plots, and chamber-hit patterns were well represented by the Monte Carlo program. Figure 9 shows the results of subjecting the generated events to all the real data analysis, including the geometrical cuts and the disposition of events with ambiguous mass, and gives the over-

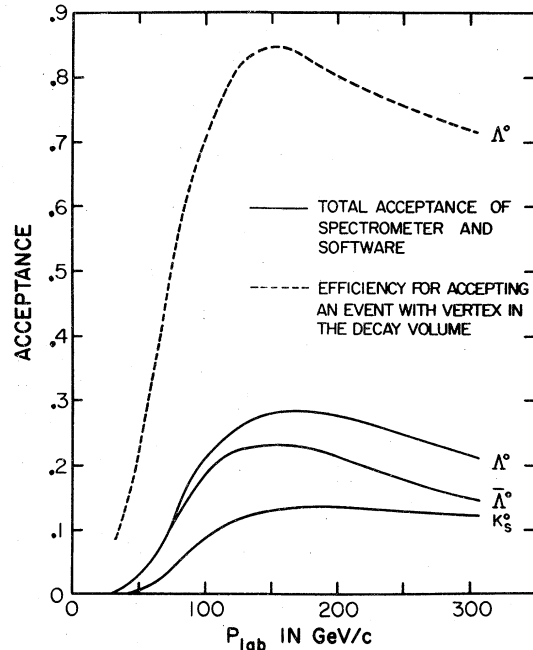


FIG. 9. Results of the Monte Carlo calculations of the over-all detection efficiency, including particle lifetime, geometrical cuts, and the treatment of invariant-mass ambiguities (see text). Table II gives the numbers. The acceptance of the spectrometer alone to Λ^0 's decaying uniformly throughout the decay volume is also shown for comparison.

TABLE II. Monte Carlo acceptance versus momentum.

$\Lambda^0 \rightarrow p\pi^-$		$K_s^0 \rightarrow \pi^+ (\text{stiff } \pi^-)$		$\bar{\Lambda}^0 \rightarrow \bar{p}\pi^+$	
p (GeV/c)	$A(p)$	p (GeV/c)	$A(p)$	p (GeV/c)	$A(p)$
35	0.0055 ± 0.0003	35	0.0002 ± 0.0001	25	0.0007 ± 0.0003
45	0.0185 ± 0.0004	45	0.0020 ± 0.0002	35	0.0057 ± 0.0005
55	0.0412 ± 0.0006	55	0.0089 ± 0.0003	45	0.0189 ± 0.0007
65	0.0720 ± 0.0009	65	0.0214 ± 0.0003	55	0.0403 ± 0.0009
75	0.1097 ± 0.0010	75	0.0388 ± 0.0004	65	0.0689 ± 0.0010
85	0.1550 ± 0.0011	85	0.0578 ± 0.0005	75	0.1023 ± 0.0012
95	0.1990 ± 0.0026	95	0.0764 ± 0.0007	85	0.1400 ± 0.0014
105	0.2190 ± 0.0029	105	0.0921 ± 0.0008	95	0.1715 ± 0.0027
115	0.2418 ± 0.0033	115	0.1045 ± 0.0009	105	0.1950 ± 0.0030
125	0.2750 ± 0.0035	125	0.1142 ± 0.0010	115	0.2135 ± 0.0035
135	0.2679 ± 0.0039	135	0.1225 ± 0.0012	125	0.2241 ± 0.0039
145	0.2758 ± 0.0040	145	0.1280 ± 0.0013	135	0.2281 ± 0.0043
155	0.2815 ± 0.0042	155	0.1315 ± 0.0015	145	0.2300 ± 0.0047
165	0.2842 ± 0.0026	165	0.1340 ± 0.0016	155	0.2302 ± 0.0050
175	0.2840 ± 0.0030	175	0.1351 ± 0.0018	165	0.2294 ± 0.0051
185	0.2820 ± 0.0033	185	0.1357 ± 0.0020	175	0.2269 ± 0.0052
195	0.2783 ± 0.0036	195	0.1355 ± 0.0022	185	0.2229 ± 0.0053
205	0.2740 ± 0.0039	205	0.1350 ± 0.0026	195	0.2167 ± 0.0052
215	0.2690 ± 0.0019	215	0.1341 ± 0.0014	205	0.2099 ± 0.0054
225	0.2635 ± 0.0045	225	0.1330 ± 0.0017	215	0.2028 ± 0.0052
235	0.2575 ± 0.0046	235	0.1316 ± 0.0019	225	0.1948 ± 0.0052
245	0.2515 ± 0.0048	245	0.1303 ± 0.0022	235	0.1876 ± 0.0053
255	0.2455 ± 0.0050	255	0.1288 ± 0.0027	245	0.1815 ± 0.0056
265	0.2393 ± 0.0054	265	0.1274 ± 0.0031	255	0.1753 ± 0.0057
275	0.2325 ± 0.0059	275	0.1259 ± 0.0040	265	0.1690 ± 0.0062
285	0.2260 ± 0.0071	285	0.1244 ± 0.0065	275	0.1633 ± 0.0068
295	0.2190 ± 0.0093	295	0.1228 ± 0.0089	285	0.1577 ± 0.0082
				295	0.1521 ± 0.0103

all efficiency including lifetime but not branching ratio, for Λ^0 , $\bar{\Lambda}^0$, and K_s^0 as a function of momentum. A plot of the Λ^0 acceptance of the spectrometer without the lifetime factor is also shown for comparison. Note that the geometrical acceptance is around 80% for Λ^0 momenta between 100 GeV/c and 300 GeV/c. The numerical values of the efficiency $A(p)$ are also given in Table II.

D. Corrections

The targets used in this experiment were nominally $\frac{1}{2}$ -interaction-length thick, and to obtain cross sections per nucleus a correction had to be made for target absorption. To study this effect, yield measurements were also made with $\frac{1}{4}$ -interaction-length targets. As shown in Fig. 10, the spectrum shapes were the same, so the target absorption correction was taken to be independent of momentum and angle. Let the $\frac{1}{2}$ -interaction-length targets have length L , the effective mean free path of the incident protons be $1/\lambda_1$, and that of the produced particles be $1/\lambda_2$. Then, because the short targets have length $L/2$, the ratio of yields $r = (\text{long target})/(\text{short target})$ is given by

$$r = e^{-\lambda_1 L/2} + e^{-\lambda_2 L/2} \quad (9)$$

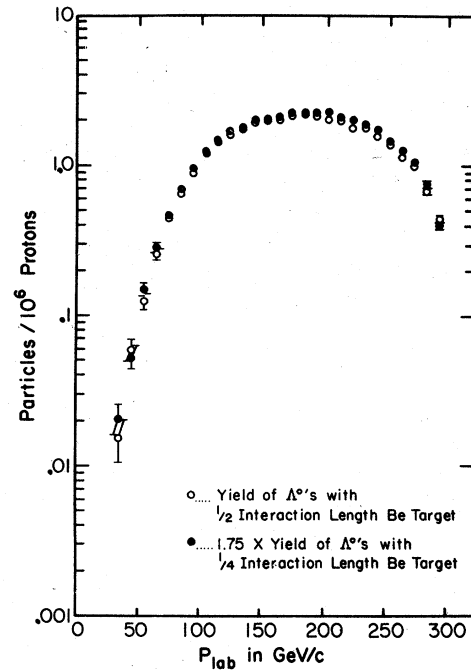


FIG. 10. Spectrum shapes observed from two different lengths of beryllium target, showing that the target absorption correction can be assumed momentum independent.

A correction factor c can be defined such that if σ' is the measured thick target cross section, the cross section per nucleus is $\sigma = c\sigma'$, and

$$c = \frac{2[\ln(r-b) - \ln b]}{r(r-2b)}, \quad (10)$$

where $b \equiv e^{-\lambda_1 L/2}$. Given $r > 1$, Eq. (10) has one free parameter b , which is bounded $(r-1) \leq b \leq 1$. For the beryllium targets, $r_{\Lambda^0} = 1.78 \pm 0.05$ and $r_{K^0} = 1.77 \pm 0.07$, so that b has a fairly narrow range to vary $0.78 \leq b \leq 1$. Over this small range the value of c is stable $c_{Be} = 1.26 \pm 0.07$. The same correction factor was used for Λ^0 , K^0 , and $\bar{\Lambda}^0$. The copper and lead corrections were $c_{Cu} = 1.20 \pm 0.07$ and $c_{Pb} = 1.17 \pm 0.07$.

One important correction was momentum dependent. Secondary sources of short-lived particles were present due to interactions of the neutral beam within the collimator, and these sources enhanced the low-momentum component of the spectra at small production angles. Particles produced in the collimator had a broader spatial distribution, and hence a wider distribution in R^2 at the target. The data remaining after the $R^2 \leq 40\text{-mm}^2$ cut discussed in Sec. B above thus contained a momentum-dependent background which at 0 mrad for Λ^0 amounted to a maximum of 10% at 60 GeV/c.

Other corrections were applied to the observed spectra, including losses due to absorption in the small amount of material in the spectrometer (+8% for Λ^0 and $\bar{\Lambda}^0$ and +6% for K^0), trigger efficiency (+1%), and target-empty backgrounds (maximum of -5% at small angles). There were also small differences in the effects of some of the cuts on the Monte Carlo when compared to the real data which were taken into account.

All of these corrections were combined into a function $C(p, \theta)$. This function is used below to obtain the cross section. Representative values are given in Table III.

E. Normalization

The differential cross section at a given angle and momentum in the laboratory in terms of the measured number of events $N(p, \theta)$ of the form shown in Fig. 7 is

$$\frac{d\sigma}{dp d\Omega} = \frac{N(p, \theta)C(p, \theta)}{A(p)IB\Delta p \Delta\Omega} \left(\frac{A}{N_{Av}\rho L} \right). \quad (11)$$

Here $C(p, \theta)$ is the correction function defined in Sec. III D, $A(p)$ is the Monte Carlo acceptance shown in Fig. 9, B is the appropriate branching ratio (0.62 for $\Lambda^0 \rightarrow p\pi^-$ and 0.687 for $K^0 \rightarrow \pi^+\pi^-$),²⁰ Δp is the momentum bin width, $\Delta\Omega$ is given by Eq. (6), $(N_{Av}\rho L/A)$ is the number of nuclei per

cm^2 , and I is the total number of incident protons which struck the target. This last quantity is defined in terms of the calibration constant given in Eq. (5) by

$$I = \frac{(\text{IC volts})f}{k_{\text{IC}}}, \quad (12)$$

where f is the fraction of the beam which strikes the target, and IC volts has been corrected for dead-time losses. The invariant cross section is then

$$E \frac{d^3\sigma}{dp^3} = \frac{E_{\text{lab}}}{p_{\text{lab}}^2} \frac{d\sigma}{dp_{\text{lab}} d\Omega}. \quad (13)$$

A sample calculation is done in the Appendix.

There are in principle three distinct types of normalization errors: (1) run to run reproducibility at the same angle with the same target, for which various secondary monitors can be used; (2) normalization between angles or for different targets, where the stability of the primary monitor, the ion chamber, or variations of beam on target as the geometry is changed are important; and (3) overall scale errors, where such factors as the defining solid angle, the absolute calibration of the primary monitor, and the validity of the target absorption correction come into play. In practice there was no difference between (1) and (2), because the primary monitor was always used. Such run to run normalization is assigned an error of $\pm 3\%$. The following errors were included in the overall scale uncertainty: (1) target absorption correction $\pm 5\%$; (2) spectrometer absorption correction $\pm 2\%$; (3) trigger efficiency $\pm 1\%$; (4) reconstruction efficiency $\pm 1\%$; ion-chamber calibration $\pm 5\%$; and solid-angle uncertainty $\pm 6\%$. Adding these in quadrature gives a scale uncertainty of $\pm 10\%$.

IV. RESULTS

A. Inclusive spectra

Momentum spectra of reconstructed Λ^0 , K^0 , and $\bar{\Lambda}^0$ at fixed laboratory angles similar to the ones shown in Fig. 7 were converted into corrected invariant cross sections per nucleus by using Eqs. (11)–(13). A portion of the results is graphically displayed in Figs. 11–16. All of the data points are given in Tables III–V. The angles shown differ slightly from the nominal deflection angle of the proton beam because of a small misalignment between the undeflected proton direction and the neutral collimator axis. The errors shown do not include the overall $\pm 10\%$ scale uncertainty discussed above. Data below 60-GeV/c laboratory momentum were cut from the final cross sections

TABLE III. Λ^0 inclusive invariant cross sections.

$\theta = 0.25$ mrad				
$Ed^3\sigma/dp^3$ (mb/GeV ²)				
p (GeV/c)	Be	Cu	Pb	$C(p, \theta)^a$ for beryllium
65	4.40 ± 0.21	17.3 ± 1.2	35.8 ± 2.3	1.25
75	4.40 ± 0.18	16.79 ± 0.97	32.1 ± 1.7	1.26
85	4.42 ± 0.16	14.72 ± 0.76	29.5 ± 1.4	1.27
95	4.39 ± 0.16	15.35 ± 0.73	28.9 ± 1.3	1.29
105	4.315 ± 0.099	14.68 ± 0.52	24.81 ± 0.84	1.28
115	4.158 ± 0.092	13.17 ± 0.45	24.03 ± 0.77	1.28
125	4.162 ± 0.090	13.36 ± 0.43	22.18 ± 0.70	1.27
135	4.091 ± 0.088	12.19 ± 0.39	21.97 ± 0.67	1.27
145	3.893 ± 0.083	11.81 ± 0.37	20.55 ± 0.62	1.27
155	3.705 ± 0.079	10.31 ± 0.33	19.38 ± 0.58	1.27
165	3.604 ± 0.073	10.14 ± 0.31	16.78 ± 0.50	1.27
175	3.510 ± 0.069	9.80 ± 0.29	16.32 ± 0.48	1.27
185	3.317 ± 0.067	8.67 ± 0.27	15.53 ± 0.46	1.27
195	3.176 ± 0.065	7.78 ± 0.25	13.73 ± 0.42	1.27
205	2.881 ± 0.061	7.76 ± 0.24	12.43 ± 0.39	1.27
215	2.724 ± 0.056	7.07 ± 0.22	11.70 ± 0.38	1.27
225	2.549 ± 0.057	6.58 ± 0.22	10.48 ± 0.35	1.27
235	2.321 ± 0.053	5.98 ± 0.21	9.89 ± 0.34	1.28
245	2.020 ± 0.048	5.16 ± 0.19	8.70 ± 0.31	1.28
255	1.758 ± 0.044	4.67 ± 0.18	7.79 ± 0.29	1.28
265	1.471 ± 0.039	3.53 ± 0.15	6.35 ± 0.26	1.29
275	1.131 ± 0.033	3.00 ± 0.14	4.50 ± 0.21	1.29
285	0.771 ± 0.026	2.02 ± 0.11	3.11 ± 0.17	1.29
295	0.451 ± 0.019	1.225 ± 0.088	2.01 ± 0.14	1.29
$\theta = 0.9$ mrad				
$Ed^3\sigma/dp^3$ (mb/GeV ²)				
p (GeV/c)	Be	Cu	Pb	
65	4.60 ± 0.19	20.2 ± 1.1	37.2 ± 2.0	
75	4.57 ± 0.15	18.46 ± 0.81	35.5 ± 1.5	
85	4.21 ± 0.12	15.80 ± 0.60	31.2 ± 1.1	
95	4.33 ± 0.11	16.33 ± 0.55	27.62 ± 0.94	
105	4.37 ± 0.10	14.74 ± 0.47	27.02 ± 0.84	
115	4.137 ± 0.096	14.01 ± 0.42	24.88 ± 0.75	
125	4.059 ± 0.092	12.63 ± 0.37	21.87 ± 0.65	
135	3.728 ± 0.085	12.33 ± 0.36	20.27 ± 0.60	
145	3.617 ± 0.081	11.05 ± 0.32	19.91 ± 0.57	
155	3.459 ± 0.007	10.17 ± 0.29	17.97 ± 0.52	
165	3.332 ± 0.071	9.81 ± 0.28	15.97 ± 0.46	
175	3.080 ± 0.077	8.79 ± 0.25	14.54 ± 0.42	
185	2.891 ± 0.062	8.39 ± 0.24	14.12 ± 0.40	
195	2.717 ± 0.059	7.70 ± 0.22	12.27 ± 0.37	
205	2.474 ± 0.055	6.81 ± 0.21	11.43 ± 0.35	
215	2.259 ± 0.049	5.98 ± 0.18	10.08 ± 0.31	
225	1.956 ± 0.047	5.60 ± 0.18	8.89 ± 0.30	
235	1.789 ± 0.045	4.90 ± 0.17	7.76 ± 0.27	
245	1.599 ± 0.041	4.25 ± 0.15	6.62 ± 0.25	
255	1.295 ± 0.035	3.51 ± 0.13	5.67 ± 0.22	
265	1.004 ± 0.031	2.84 ± 0.12	4.17 ± 0.19	
275	0.772 ± 0.025	2.055 ± 0.098	3.54 ± 0.17	
285	0.510 ± 0.020	1.384 ± 0.080	2.26 ± 0.13	
295	0.288 ± 0.015	0.854 ± 0.064	1.42 ± 0.11	

TABLE III. (Continued)

$\theta = 1.2 \text{ mrad}$			
$Ed^3\sigma/dp^3 \text{ (mb/GeV}^2\text{)}$			
p (GeV/c)	Be	Cu	Pb
65	4.63 ± 0.17	18.11 ± 0.79	35.9 ± 1.9
75	4.42 ± 0.14	17.17 ± 0.62	33.0 ± 1.4
85	4.06 ± 0.11	15.46 ± 0.49	29.5 ± 1.1
95	4.10 ± 0.11	14.87 ± 0.44	28.33 ± 0.98
105	3.96 ± 0.10	14.34 ± 0.40	24.60 ± 0.82
115	3.905 ± 0.096	13.45 ± 0.37	23.32 ± 0.75
125	3.757 ± 0.091	12.41 ± 0.34	21.24 ± 0.67
135	3.581 ± 0.077	12.10 ± 0.29	19.43 ± 0.57
145	3.411 ± 0.073	10.40 ± 0.26	17.71 ± 0.52
155	3.253 ± 0.069	9.91 ± 0.24	16.76 ± 0.49
165	3.085 ± 0.063	9.05 ± 0.22	14.90 ± 0.42
175	2.859 ± 0.057	8.20 ± 0.19	13.95 ± 0.40
185	2.712 ± 0.055	7.40 ± 0.18	12.09 ± 0.36
195	2.486 ± 0.052	6.68 ± 0.17	10.67 ± 0.33
205	2.172 ± 0.047	6.07 ± 0.16	10.05 ± 0.32
215	1.997 ± 0.042	5.47 ± 0.14	8.82 ± 0.28
225	1.798 ± 0.041	4.76 ± 0.13	8.07 ± 0.28
235	1.552 ± 0.037	4.04 ± 0.12	6.64 ± 0.24
245	1.345 ± 0.034	3.56 ± 0.11	5.79 ± 0.22
255	1.106 ± 0.029	2.883 ± 0.095	4.27 ± 0.18
265	0.878 ± 0.025	2.076 ± 0.078	3.74 ± 0.17
275	0.607 ± 0.019	1.551 ± 0.065	2.37 ± 0.13
285	0.417 ± 0.016	1.114 ± 0.055	2.06 ± 0.12
295	0.223 ± 0.011	0.551 ± 0.037	1.136 ± 0.091

$\theta = 1.5 \text{ mrad}$			
$Ed^3\sigma/dp^3 \text{ (mb/GeV}^2\text{)}$			
p (GeV/c)	Be	Cu	Pb
65	4.55 ± 0.17	20.1 ± 1.0	36.0 ± 1.8
75	4.13 ± 0.13	16.57 ± 0.70	32.7 ± 1.3
85	4.01 ± 0.10	15.29 ± 0.54	28.77 ± 0.98
95	3.962 ± 0.098	14.36 ± 0.47	26.02 ± 0.83
105	3.768 ± 0.089	13.74 ± 0.41	24.41 ± 0.73
115	3.694 ± 0.084	12.62 ± 0.37	21.56 ± 0.63
125	3.417 ± 0.076	11.38 ± 0.33	19.97 ± 0.57
135	3.327 ± 0.074	10.07 ± 0.29	17.93 ± 0.51
145	3.126 ± 0.069	9.76 ± 0.28	16.76 ± 0.48
155	2.825 ± 0.063	8.54 ± 0.24	14.66 ± 0.42
165	2.555 ± 0.055	7.88 ± 0.22	13.77 ± 0.39
175	2.472 ± 0.052	7.42 ± 0.21	12.29 ± 0.35
185	2.211 ± 0.047	6.50 ± 0.19	10.95 ± 0.32
195	1.987 ± 0.044	5.78 ± 0.17	9.41 ± 0.29
205	1.783 ± 0.041	5.24 ± 0.16	8.22 ± 0.26
215	1.557 ± 0.035	4.47 ± 0.14	7.08 ± 0.23
225	1.324 ± 0.033	3.97 ± 0.13	6.23 ± 0.22
235	1.115 ± 0.029	3.31 ± 0.12	4.99 ± 0.19
245	0.937 ± 0.026	2.79 ± 0.11	4.11 ± 0.17
255	0.713 ± 0.021	2.174 ± 0.092	3.39 ± 0.15
265	0.552 ± 0.018	1.706 ± 0.080	2.84 ± 0.14
275	0.379 ± 0.014	1.232 ± 0.066	1.90 ± 0.11
285	0.239 ± 0.011	0.742 ± 0.051	1.255 ± 0.087
295	0.1166 ± 0.0073	0.415 ± 0.037	0.643 ± 0.062

TABLE III. (Continued)

p (GeV/c)	$\theta = 2.9$ mrad		$\theta = 3.6$ mrad			
	$Ed^3\sigma/dp^3$ (mb/GeV ²)					
	Be		Pb			
65	3.85	± 0.12	34.8	± 1.4	3.57	± 0.20
75	3.665	± 0.091	28.83	± 0.97	3.58	± 0.15
85	3.345	± 0.071	24.32	± 0.71	3.02	± 0.11
95	3.169	± 0.065	21.97	± 0.61	2.888	± 0.097
105	2.946	± 0.058	18.77	± 0.50	2.742	± 0.084
115	2.702	± 0.052	16.47	± 0.43	2.469	± 0.073
125	2.383	± 0.045	14.63	± 0.38	2.176	± 0.064
135	2.246	± 0.043	12.51	± 0.33	1.812	± 0.055
145	1.936	± 0.037	10.96	± 0.29	1.565	± 0.048
155	1.718	± 0.038	9.07	± 0.27	1.335	± 0.045
165	1.443	± 0.028	7.19	± 0.21	1.120	± 0.037
175	1.264	± 0.024	5.98	± 0.18	0.887	± 0.031
185	1.027	± 0.021	5.06	± 0.16	0.721	± 0.027
195	0.890	± 0.019	4.04	± 0.14	0.532	± 0.022
205	0.710	± 0.016	3.11	± 0.12	0.465	± 0.021
215	0.547	± 0.013	2.45	± 0.10	0.301	± 0.016
225	0.420	± 0.012	1.818	± 0.085	0.258	± 0.015
235	0.3133	± 0.0095	1.260	± 0.069	0.162	± 0.011
245	0.2290	± 0.0078	1.019	± 0.061	0.1200	± 0.0096
255	0.1618	± 0.0063	0.698	± 0.050	0.0639	± 0.0068
265	0.0966	± 0.0047	0.476	± 0.040	0.0534	± 0.0062
275	0.0575	± 0.0035	0.249	± 0.028	0.0188	± 0.0035
285	0.0363	± 0.0028	0.194	± 0.025		
295	0.0152	± 0.0017	0.082	± 0.016		

p (GeV/c)	$\theta = 5.0$ mrad		$C(p, \theta)$ for beryllium		
	$Ed^3\sigma/dp^3$ (mb/GeV ²)				
	Be	Pb			
65	3.222	± 0.074	26.65	± 0.99	1.37
75	2.907	± 0.056	23.14	± 0.71	1.40
85	2.405	± 0.042	18.10	± 0.50	1.36
95	2.086	± 0.038	15.10	± 0.41	1.35
105	1.728	± 0.030	12.16	± 0.32	1.34
115	1.451	± 0.026	9.49	± 0.26	1.33
125	1.160	± 0.021	7.52	± 0.21	1.33
135	0.941	± 0.017	5.71	± 0.17	1.32
145	0.740	± 0.014	4.56	± 0.14	1.32
155	0.571	± 0.013	3.36	± 0.12	1.32
165	0.4153	± 0.0085	2.591	± 0.094	1.31
175	0.3150	± 0.0067	1.590	± 0.069	1.30
185	0.2170	± 0.0052	1.334	± 0.061	1.29
195	0.1571	± 0.0042	0.911	± 0.049	1.28
205	0.1104	± 0.0034	0.640	± 0.040	1.26
215	0.0687	± 0.0025	0.414	± 0.031	1.24
225	0.0503	± 0.0021	0.260	± 0.024	1.22
235	0.0282	± 0.0015	0.155	± 0.018	1.17
245	0.0164	± 0.0011	0.058	± 0.011	1.10
255	0.00865	± 0.00079	0.0372	± 0.0091	1.00
265	0.00362	± 0.00052	0.0221	± 0.0074	0.82
275	0.00154	± 0.00038			0.63

TABLE III. (Continued)

$\theta = 6.9 \text{ mrad}$ $Ed^3\sigma/dp^3 \text{ (mb/GeV}^2\text{)}$				
p (GeV/c)	Be		Pb	
65	2.670	± 0.063	25.88	± 0.84
75	2.178	± 0.044	19.98	± 0.56
85	1.674	± 0.031	13.54	± 0.36
95	1.284	± 0.025	10.10	± 0.27
105	0.953	± 0.019	7.39	± 0.20
115	0.697	± 0.014	5.24	± 0.15
125	0.503	± 0.011	3.79	± 0.12
135	0.3473	± 0.0080	2.500	± 0.088
145	0.2429	± 0.0061	1.732	± 0.069
155	0.1606	± 0.0048	1.218	± 0.056
165	0.1060	± 0.0033	0.717	± 0.039
175	0.0625	± 0.0023	0.432	± 0.028
185	0.0400	± 0.0018	0.282	± 0.022
195	0.0220	± 0.0013	0.131	± 0.014
205	0.01190	± 0.00092	0.077	± 0.011
215	0.00547	± 0.00065	0.242	± 0.0078
225	0.00327	± 0.00054		
235	0.00164	± 0.00046		

$\theta = 8.8 \text{ mrad}$ $Ed^3\sigma/dp^3 \text{ (mb/GeV}^2\text{)}$							
p (GeV/c)	Be	Cu	Pb	$C(p, \theta)$ for Be			
65	2.098	± 0.047	9.65	± 0.35	20.40	± 0.64	1.40
75	1.613	± 0.032	6.61	± 0.22	13.77	± 0.39	1.41
85	1.051	± 0.020	4.44	± 0.14	8.75	± 0.25	1.36
95	0.725	± 0.015	3.11	± 0.10	5.94	± 0.17	1.34
105	0.499	± 0.010	1.916	± 0.068	4.22	± 0.13	1.33
115	0.3163	± 0.0072	1.199	± 0.048	2.625	± 0.089	1.32
125	0.2180	± 0.0053	0.759	± 0.035	1.774	± 0.066	1.32
135	0.1242	± 0.0036	0.479	± 0.026	1.024	± 0.046	1.32
145	0.0792	± 0.0026	0.304	± 0.019	0.652	± 0.035	1.33
155	0.0457	± 0.0019	0.179	± 0.014	0.431	± 0.027	1.33
165	0.0245	± 0.0012	0.0948	± 0.0093	0.223	± 0.018	1.18
175	0.01455	± 0.00091	0.0480	± 0.0063	0.116	± 0.012	1.09
185	0.00507	± 0.00057	0.0136	± 0.0038	0.0447	± 0.0079	0.83
195	0.00235	± 0.00046	0.0133	± 0.0036			0.60

^a Representative values of the correction factor defined in Sec. III D are given for Λ^0 production for the Be target. The corrections for the other targets and for K_s^0 and $\bar{\Lambda}^0$ production do not vary more than ± 20 percent.

because of the errors resulting from poor statistics and large corrections for decay in the collimator. This cut limited Feynman $x \geq 0.2$. The forward cross section for Λ^0 production is rather flat in x for $x < 0.8$ or so, especially from beryllium, while the K_s^0 cross section falls monotonically with increasing x . The $\bar{\Lambda}^0$ cross sections falls even more steeply as x increases than does the K_s^0 . For a given target at small x the K_s^0 and

Λ^0 cross sections are comparable while the $\bar{\Lambda}^0$ cross sections are a factor of 10 smaller. The cross sections all decrease with increasing production angle, an effect which is more pronounced as x increases.

The cross sections per nucleus obviously depend on the atomic weight of the target. The spectrum shapes are also A dependent, however, as is apparent by comparing the forward angle Λ^0 spec-

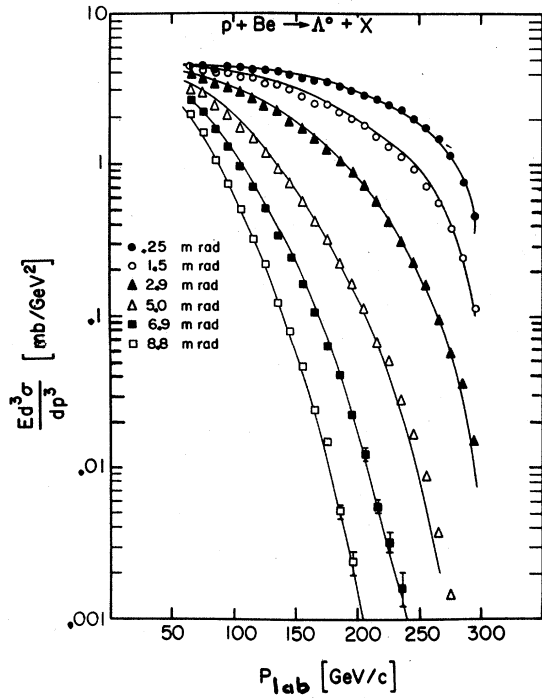


FIG. 11. Invariant cross sections for Λ^0/Σ^0 production by 300-GeV protons per beryllium nucleus. The curves here and in Figs. 12–16 were generated by using the fit parameters given in Table VI and the fixed angles in the laboratory shown in the figure.

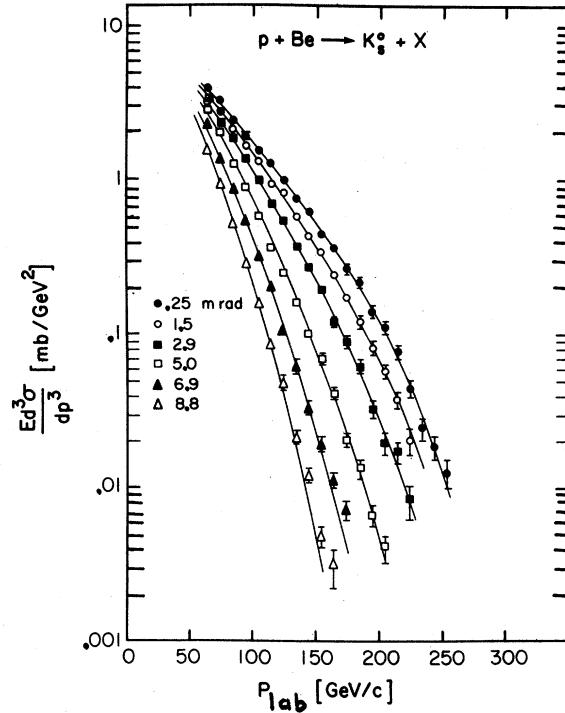


FIG. 13. Invariant cross sections for K_S^0 production by 300-GeV protons per beryllium nucleus.

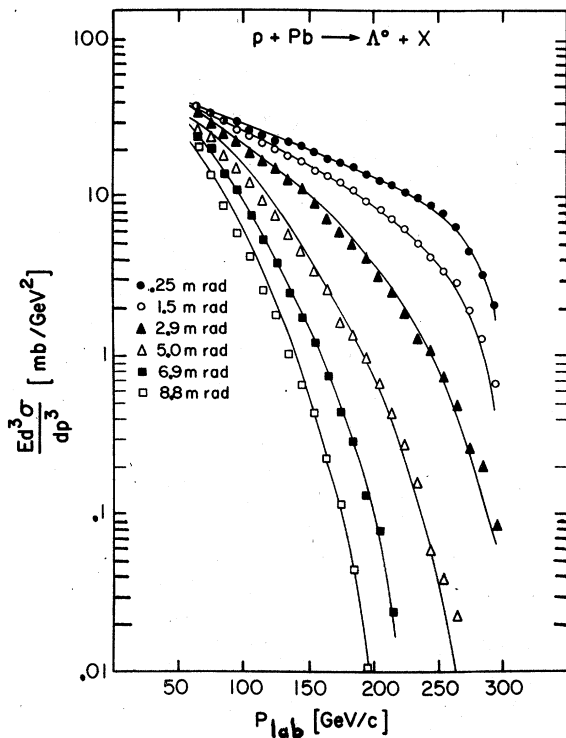


FIG. 12. Invariant cross sections for Λ^0/Σ^0 production by 300-GeV protons per lead nucleus.

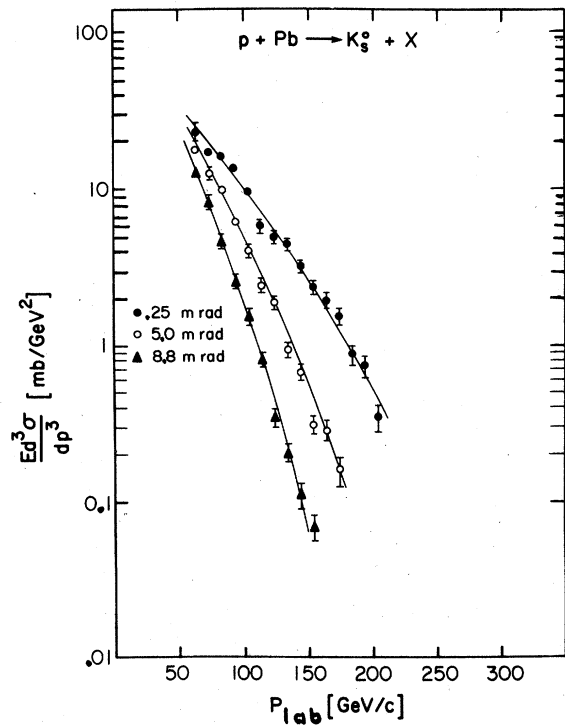


FIG. 14. Invariant cross sections for K_S^0 production by 300-GeV protons per lead nucleus.

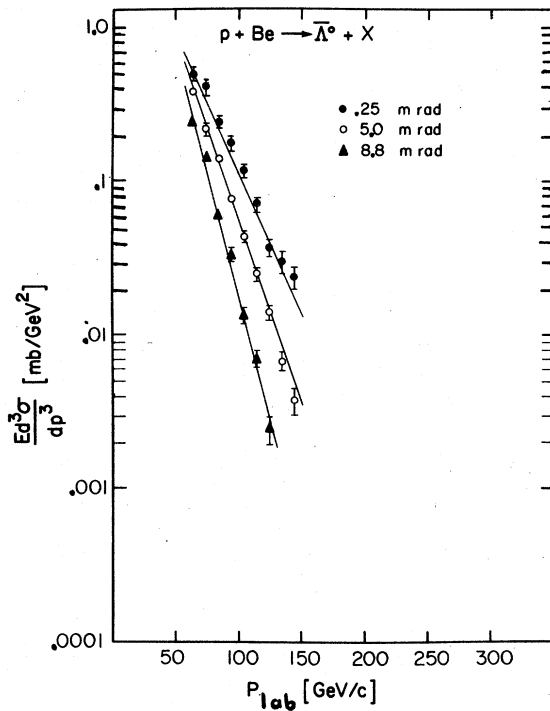


FIG. 15. Invariant cross sections for $\bar{\Lambda}^0$ production by 300-GeV protons per beryllium nucleus.

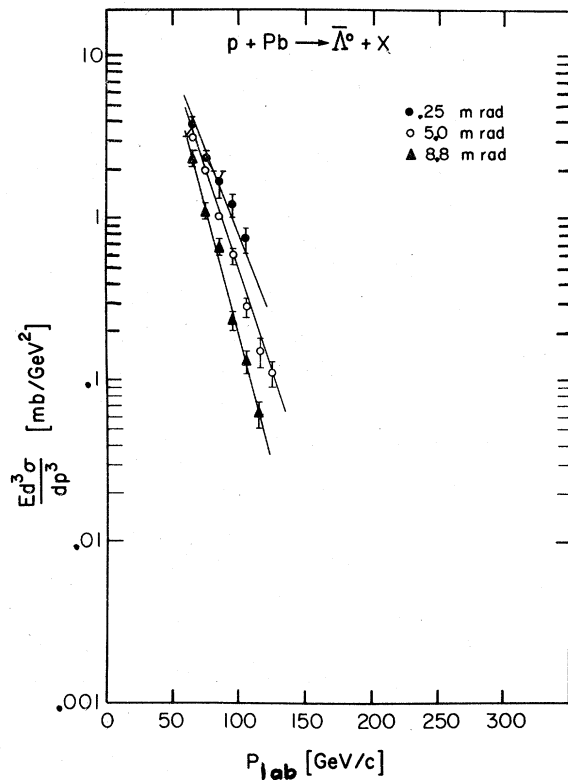


FIG. 16. Invariant cross sections for $\bar{\Lambda}^0$ production by 300-GeV protons per lead nucleus.

tra from beryllium and lead (Figs. 11 and 12). This A dependence can be expressed in terms of a power law of the form

$$E \frac{d^3\sigma}{dp^3}(A) = A^\alpha E \frac{d^3\sigma}{dp^3}(A=1), \quad (14)$$

where the exponent α can depend on the kinematic variables.²² Figure 17 shows several (x, p_\perp) data points for each of the three targets on a log-log plot, and demonstrates that the results are consistent with Eq. (14). The slope α is not a constant (x, p_\perp) are varied. The extrapolation to $A=1$ gives the "nucleon" cross section for that value of (x, p_\perp) . In this manner the beryllium and lead data were used to generate "nucleon data" points.

To express the cross sections as smooth functions of the scaling variables (x, p_\perp) , the beryllium, lead, and "nucleon" fixed angle data were empirically fitted. The empirical functional form, the parameters determined by the fitting procedure, and the resulting χ^2 are shown in Table VI. These fits calculated at constant angles are compared to the data in Figs. 11 through 16. The fits give reliable expressions for the data over the kinematic region covered by the measurements, but do not necessarily give true extrapolations into regions not actually measured— $x=0$, for example. The nucleon results are of course entirely

extrapolations via Eq. (14) which, although seemingly valid for complex nuclei, has not been demonstrated to give the correct cross section at $A=1$.

Figures 18 through 23 show the fits plotted in terms of the scaling variables. The first three plots show the quantity $(A^{-2/3} E d^3\sigma / dp^3)$ versus x with p_\perp^2 as a parameter, while the next three show the same quantity versus p_\perp^2 with x as a parameter. The separation of the variables $E d^3\sigma / dp^3 = f_1(x) f_2(p_\perp^2)$ does not work well for the Λ^0 spectra, where the slope in x becomes steeper as p_\perp^2 increases, but is more nearly valid for the K_S^0 spectra. It is apparent from these curves that the x dependence varies considerably with particle type, falling more steeply with increasing x for K_S^0 than for Λ^0 , and more steeply for $\bar{\Lambda}^0$ than for K_S^0 .²³ The slow falloff of the Λ^0 spectrum as $x \rightarrow 1$ is characteristic of the leading particle effect, also exhibited by the Σ^- hyperon.^{14,15} K mesons can be produced in association with hyperons, but carry a smaller fraction of the parent proton momentum. Anti-hyperons are produced in pairs with hyperons, predominantly in the central region with small x . In contrast to the x dependence, the three particles show very similar fall off at fixed

TABLE IV. K_s^0 inclusive invariant cross sections.

$\theta = 0.25$ mrad			
$Ed^3\sigma/dp^3$ (mb/GeV ²)			
p (GeV/c)	Be	Cu	Pb
65	3.83 ± 0.30	16.6 ± 2.0	22.7 ± 2.9
75	3.11 ± 0.20	11.3 ± 1.2	16.8 ± 1.7
85	2.36 ± 0.14	8.65 ± 0.81	16.1 ± 1.4
95	1.933 ± 0.088	6.42 ± 0.53	13.2 ± 1.1
105	1.552 ± 0.069	3.87 ± 0.35	9.47 ± 0.70
115	1.270 ± 0.056	4.13 ± 0.33	5.85 ± 0.49
125	0.984 ± 0.044	2.99 ± 0.26	5.03 ± 0.41
135	0.740 ± 0.035	2.14 ± 0.20	4.40 ± 0.36
145	0.613 ± 0.030	1.55 ± 0.16	3.21 ± 0.29
155	0.435 ± 0.023	1.43 ± 0.14	2.36 ± 0.23
165	0.358 ± 0.020	1.00 ± 0.11	1.96 ± 0.20
175	0.263 ± 0.016	0.637 ± 0.088	1.55 ± 0.17
185	0.212 ± 0.014	0.490 ± 0.075	0.87 ± 0.12
195	0.139 ± 0.011	0.368 ± 0.063	0.74 ± 0.11
205	0.1099 ± 0.0095	0.241 ± 0.050	0.343 ± 0.074
215	0.0758 ± 0.0075	0.240 ± 0.048	
225	0.0437 ± 0.0056		
235	0.0237 ± 0.0040		
245	0.0179 ± 0.0034		
255	0.0124 ± 0.0028		

$\theta = 0.9$ mrad			
$Ed^3\sigma/dp^3$ (mb/GeV ²)			
p (GeV/c)	Be	Cu	Pb
65	3.57 ± 0.30	14.3 ± 1.6	24.9 ± 2.9
75	2.92 ± 0.20	10.21 ± 0.97	19.1 ± 1.8
85	2.26 ± 0.14	8.32 ± 0.70	16.2 ± 1.3
95	1.68 ± 0.10	6.16 ± 0.45	11.13 ± 0.81
105	1.493 ± 0.072	4.79 ± 0.35	8.86 ± 0.62
115	1.219 ± 0.058	3.89 ± 0.28	6.03 ± 0.46
125	0.973 ± 0.047	3.03 ± 0.22	4.75 ± 0.37
135	0.721 ± 0.037	2.31 ± 0.18	4.13 ± 0.32
145	0.609 ± 0.032	1.55 ± 0.14	3.42 ± 0.27
155	0.437 ± 0.025	1.11 ± 0.11	2.18 ± 0.20
165	0.298 ± 0.020	0.99 ± 0.10	1.46 ± 0.16
175	0.243 ± 0.017	0.743 ± 0.083	1.08 ± 0.13
185	0.192 ± 0.015	0.480 ± 0.064	0.86 ± 0.11
195	0.119 ± 0.011	0.355 ± 0.054	0.593 ± 0.092
205	0.0644 ± 0.0078	0.285 ± 0.047	0.435 ± 0.077
215	0.0447 ± 0.0063	0.246 ± 0.043	0.277 ± 0.059
225	0.0265 ± 0.0047		
235	0.0289 ± 0.0049		
245	0.0170 ± 0.0037		

$\theta = 1.2$ mrad			
$Ed^3\sigma/dp^3$ (mb/GeV ²)			
p (GeV/c)	Be	Cu	Pb
65	3.51 ± 0.26	14.9 ± 1.3	22.8 ± 2.6
75	2.81 ± 0.18	10.15 ± 0.76	17.9 ± 1.7
85	2.45 ± 0.14	7.92 ± 0.54	15.0 ± 1.2
95	1.754 ± 0.099	6.12 ± 0.34	10.57 ± 0.85
105	1.403 ± 0.061	4.56 ± 0.26	7.83 ± 0.57
115	1.087 ± 0.048	3.36 ± 0.19	6.49 ± 0.47

TABLE IV. (Continued)

$\theta = 1.2 \text{ mrad}$			
$Ed^3\sigma/dp^3 \text{ (mb/GeV}^2\text{)}$			
p (GeV/c)	Be	Cu	Pb
125	0.820 ± 0.037	2.80 ± 0.16	4.72 ± 0.36
135	0.709 ± 0.032	2.24 ± 0.13	3.32 ± 0.28
145	0.470 ± 0.024	1.395 ± 0.097	2.41 ± 0.22
155	0.395 ± 0.021	1.082 ± 0.081	1.71 ± 0.18
165	0.304 ± 0.017	0.947 ± 0.073	1.70 ± 0.17
175	0.250 ± 0.015	0.703 ± 0.060	1.13 ± 0.13
185	0.147 ± 0.011	0.467 ± 0.047	0.628 ± 0.095
195	0.1090 ± 0.0089	0.301 ± 0.036	0.552 ± 0.086
205	0.0779 ± 0.0073	0.255 ± 0.033	0.330 ± 0.065
215	0.0549 ± 0.0059	0.119 ± 0.022	0.278 ± 0.058
225	0.0423 ± 0.0051	0.096 ± 0.019	
235	0.0208 ± 0.0035		
245	0.0131 ± 0.0027		

$\theta = 1.5 \text{ mrad}$			
$Ed^3\sigma/dp^3 \text{ (mb/GeV}^2\text{)}$			
p (GeV/c)	Be	Cu	Pb
65	3.21 ± 0.26	11.4 ± 1.3	25.1 ± 2.6
75	2.73 ± 0.18	8.65 ± 0.81	17.3 ± 1.5
85	2.04 ± 0.13	6.82 ± 0.57	15.0 ± 1.2
95	1.650 ± 0.097	7.02 ± 0.44	9.67 ± 0.76
105	1.308 ± 0.061	4.55 ± 0.31	7.76 ± 0.53
115	0.947 ± 0.046	3.20 ± 0.23	5.99 ± 0.41
125	0.821 ± 0.039	2.54 ± 0.19	4.96 ± 0.34
135	0.566 ± 0.029	1.64 ± 0.14	3.62 ± 0.27
145	0.433 ± 0.024	1.26 ± 0.11	2.36 ± 0.20
155	0.341 ± 0.020	1.080 ± 0.099	1.54 ± 0.15
165	0.238 ± 0.016	0.960 ± 0.089	1.52 ± 0.15
175	0.172 ± 0.013	0.597 ± 0.067	1.11 ± 0.12
185	0.119 ± 0.010	0.380 ± 0.052	0.592 ± 0.085
195	0.0800 ± 0.0080	0.281 ± 0.043	0.392 ± 0.067
205	0.0567 ± 0.0065	0.243 ± 0.039	0.288 ± 0.056
215	0.0373 ± 0.0051		
225	0.0196 ± 0.0036		

$\theta = 2.9 \text{ mrad}$		$\theta = 3.6 \text{ mrad}$	
$Ed^3\sigma/dp^3 \text{ (mb/GeV}^2\text{)}$			
p (GeV/c)	Be	Pb	Be
65	3.38 ± 0.19	27.1 ± 2.2	3.01 ± 0.33
75	2.32 ± 0.11	18.8 ± 1.2	2.23 ± 0.20
85	1.841 ± 0.078	14.38 ± 0.84	1.77 ± 0.13
95	1.365 ± 0.055	8.61 ± 0.53	1.335 ± 0.094
105	0.989 ± 0.041	6.43 ± 0.39	0.805 ± 0.062
115	0.678 ± 0.029	4.47 ± 0.29	0.611 ± 0.048
125	0.538 ± 0.024	3.35 ± 0.23	0.474 ± 0.039
135	0.365 ± 0.018	2.34 ± 0.16	0.307 ± 0.029
145	0.271 ± 0.014	1.56 ± 0.13	0.187 ± 0.021
155	0.193 ± 0.011	1.05 ± 0.10	0.176 ± 0.019
165	0.1215 ± 0.0084	0.624 ± 0.075	0.099 ± 0.014
175	0.0886 ± 0.0068	0.401 ± 0.058	0.0495 ± 0.0094
185	0.0604 ± 0.0054	0.323 ± 0.050	
195	0.0328 ± 0.0038	0.181 ± 0.036	
205	0.0194 ± 0.0028	0.159 ± 0.033	
215	0.0166 ± 0.0026		
225	0.0082 ± 0.0018		

TABLE IV. (Continued)

p (GeV/c)	$\theta = 5.0$ mrad		$\theta = 6.9$ mrad	
	$Ed^3\sigma/dp^3$ (mb/GeV ²)			
	Be	Pb	Be	Pb
65	2.77 ± 0.12	18.7 ± 1.4	2.233 ± 0.096	18.1 ± 1.2
75	2.005 ± 0.071	12.57 ± 0.80	1.345 ± 0.052	10.95 ± 0.64
85	1.248 ± 0.043	9.78 ± 0.56	0.842 ± 0.031	7.00 ± 0.39
95	0.868 ± 0.029	6.00 ± 0.35	0.534 ± 0.020	3.87 ± 0.23
105	0.586 ± 0.020	3.99 ± 0.25	0.319 ± 0.013	2.60 ± 0.16
115	0.364 ± 0.014	2.45 ± 0.17	0.1983 ± 0.0089	1.54 ± 0.11
125	0.253 ± 0.010	1.91 ± 0.14	0.1059 ± 0.0057	0.781 ± 0.071
135	0.1613 ± 0.0072	0.951 ± 0.087	0.0624 ± 0.0039	0.594 ± 0.057
145	0.1005 ± 0.0052	0.685 ± 0.070	0.0329 ± 0.0026	0.242 ± 0.034
155	0.0672 ± 0.0040	0.312 ± 0.044	0.0189 ± 0.0019	0.173 ± 0.027
165	0.0398 ± 0.0028	0.291 ± 0.040	0.0111 ± 0.0013	0.087 ± 0.018
175	0.0204 ± 0.0019	0.163 ± 0.029	0.0071 ± 0.0010	
185	0.0133 ± 0.0015			
195	0.0065 ± 0.0010			
205	0.00401 ± 0.0075			

p (GeV/c)	$\theta = 8.8$ mrad		
	$Ed^3\sigma/dp^3$ (mb/GeV ²)		
	Be	Cu	Pb
65	1.546 ± 0.067	6.09 ± 0.48	12.45 ± 0.84
75	0.909 ± 0.035	2.95 ± 0.22	8.00 ± 0.47
85	0.522 ± 0.020	1.97 ± 0.14	4.75 ± 0.27
95	0.288 ± 0.012	1.261 ± 0.091	2.63 ± 0.16
105	0.1541 ± 0.0072	0.675 ± 0.057	1.57 ± 0.11
115	0.0862 ± 0.0046	0.381 ± 0.038	0.817 ± 0.068
125	0.0478 ± 0.0031	0.144 ± 0.021	0.354 ± 0.040
135	0.0207 ± 0.0018	0.115 ± 0.017	0.209 ± 0.029
145	0.0118 ± 0.0013	0.057 ± 0.012	0.111 ± 0.019
155	0.00474 ± 0.00077		0.067 ± 0.014
165	0.00313 ± 0.00057		

x with increasing transverse momentum. A simple exponential in p_{\perp}^2 at constant x is not a very good approximation to the shapes for Λ^0 and K_S^0 , where the slopes of the spectra are observed to be steeper at small p_{\perp}^2 .

Another way of displaying the similarity of the cross sections as a function of p_{\perp} is to plot cross-section ratios versus x (or laboratory momentum) for the various laboratory angles. Such plots can be made with the fixed-angle data directly, and are insensitive to experimental errors, since many effects tend to cancel in the ratio. Varying the angle at fixed p_{lab} varies p_{\perp} , so the particle ratios plotted this way should depend only on p_{lab} and not on θ if the p_{\perp} dependences of the various inclusive

cross sections are the same. Figures 24 and 25 show the ratio $(p + A \rightarrow K_S^0 + X)/(p + A \rightarrow \Lambda^0 + X)$ for beryllium and lead as a function of momentum, and Figs. 26 and 27 give the corresponding data for $(p + A \rightarrow \bar{\Lambda}^0 + X)/(p + A \rightarrow \Lambda^0 + X)$. The evident independence of these ratios on production angle confirms the claim that the dependences of the cross sections on p_{\perp} are substantially the same. The same straight line is plotted on Figs. 24 and 25 to indicate that the particle ratio is not a strong function of A either. There are slight differences between the beryllium and lead ratios, however, especially at large x . A different line is plotted on Figs. 26 and 27 to show the A independence of the $\bar{\Lambda}/\Lambda$ ratio. Although extrapolation

TABLE V. $\bar{\Lambda}^0$ inclusive invariant cross sections.

$\theta = 0.25$ mrad $Ed^3\sigma/dp^3$ (mb/GeV ²)				$\theta = 3.6$ mrad $Ed^3\sigma/dp^3$ (mb/GeV ²)			$\theta = 5.0$ mrad $Ed^3\sigma/dp^3$ (mb/GeV ²)	
p (GeV/c)	Be	Cu	Pb	p (GeV/c)	Be	Be	Pb	
65	0.488 ± 0.055	2.49 ± 0.32	3.64 ± 0.68	65	0.307 ± 0.060	0.373 ± 0.024	3.10 ± 0.33	
75	0.393 ± 0.038	1.10 ± 0.16	2.22 ± 0.40	75	0.355 ± 0.050	0.212 ± 0.014	1.94 ± 0.21	
85	0.234 ± 0.023	0.71 ± 0.10	1.64 ± 0.27	85	0.257 ± 0.034	0.1392 ± 0.0088	1.00 ± 0.12	
95	0.173 ± 0.017	0.579 ± 0.078	1.19 ± 0.20	95	0.105 ± 0.018	0.0769 ± 0.0054	0.577 ± 0.074	
105	0.116 ± 0.012	0.318 ± 0.051	0.73 ± 0.14	105	0.066 ± 0.013	0.0426 ± 0.0034	0.277 ± 0.045	
115	0.0705 ± 0.0085	0.169 ± 0.034		115	0.0465 ± 0.0096	0.0255 ± 0.0024	0.148 ± 0.030	
125	0.0378 ± 0.0057	0.124 ± 0.027		125		0.0141 ± 0.0016	0.109 ± 0.024	
135	0.0304 ± 0.0049			135		0.0068 ± 0.0010		
145	0.0241 ± 0.0042			145		0.00371 ± 0.00073		

$\theta = 1.2$ mrad $Ed^3\sigma/dp^3$ (mb/GeV ²)				$\theta = 6.9$ mrad $Ed^3\sigma/dp^3$ (mb/GeV ²)		
p (GeV/c)	Be	Cu	Pb	p (GeV/c)	Be	Pb
65	0.517 ± 0.062	2.05 ± 0.36	4.16 ± 0.66	65	0.335 ± 0.021	2.65 ± 0.26
75	0.343 ± 0.038	1.03 ± 0.19	3.02 ± 0.43	75	0.173 ± 0.011	1.65 ± 0.16
85	0.205 ± 0.023	0.82 ± 0.13	1.19 ± 0.21	85	0.096 ± 0.007	0.852 ± 0.089
95	0.127 ± 0.016	0.565 ± 0.093	0.95 ± 0.16	95	0.051 ± 0.004	0.367 ± 0.049
105	0.106 ± 0.013	0.285 ± 0.058	0.52 ± 0.10	105	0.026 ± 0.002	0.208 ± 0.032
115	0.0640 ± 0.0088	0.243 ± 0.049	0.508 ± 0.094	115	0.014 ± 0.002	0.146 ± 0.024
125	0.0366 ± 0.0062			125	0.0055 ± 0.0009	
135	0.0253 ± 0.0049			135	0.0033 ± 0.0007	

$\theta = 2.9$ mrad $Ed^3\sigma/dp^3$ (mb/GeV ²)			$\theta = 8.8$ mrad $Ed^3\sigma/dp^3$ (mb/GeV ²)			
p (GeV/c)	Be	Pb	p (GeV/c)	Be	Cu	Pb
65	0.414 ± 0.039	4.13 ± 0.49	65	0.240 ± 0.015	1.16 ± 0.12	2.30 ± 0.21
75	0.250 ± 0.023	2.02 ± 0.26	75	0.1386 ± 0.0087	0.604 ± 0.067	1.08 ± 0.11
85	0.185 ± 0.016	1.29 ± 0.16	85	0.0610 ± 0.0043	0.195 ± 0.029	0.657 ± 0.067
95	0.124 ± 0.011	0.70 ± 0.10	95	0.0336 ± 0.0027	0.122 ± 0.020	0.233 ± 0.033
105	0.0667 ± 0.0069	0.480 ± 0.074	105	0.0135 ± 0.0014		0.130 ± 0.022
115	0.0452 ± 0.0051		115	0.00696 ± 0.00092		0.061 ± 0.013
125	0.0222 ± 0.0033		125	0.00239 ± 0.00050		
135	0.0153 ± 0.0026					

to $x=0$ is risky, it is amusing that both plots are consistent with $\bar{\Lambda} = \Lambda$ in the central region.

B. A dependence

The A dependence of the Λ^0 spectra has been discussed in Ref. 9 in terms of a collision model, where the excited projectile system which produces the observed Λ^0 loses longitudinal momentum and gains transverse momentum by collisions as it leaves the nucleus. In this view the incident projectile is excited by one collision, scatters by other collisions, and becomes a definite num-

ber of final-state particles after it has left the nuclear volume.²⁴ It is convenient to express the longitudinal momentum in terms of rapidity

$$y = \frac{1}{2} \ln[(E+p_{\parallel})/(E-p_{\parallel})]. \quad (15)$$

Then the invariant phase-space volume loses its energy denominator

$$\frac{d^3p}{E} = \pi dy dp_{\perp}^2, \quad (16)$$

and phase space is uniformly weighted in y . The differential multiplicity defined by Eq. (3) in

TABLE VI. Parameters from the empirical fit to the data in the form

$$f(x, p_T) = e^{c_1 + c_2 x^2 + c_3 x + c_4 p_T + c_5 p_T^2 + c_6 p_T^4 + c_7 p_T^6} (1-x)^{c_8 + c_9 p_T^2}$$

Parameter	Λ^0			$\bar{\Lambda}^0$			K_S^0		
	Be	Pb	Nucleon	Be	Pb	Nucleon	Be	Pb	Nucleon
c_1	1.45 ± 0.02	4.11 ± 0.03	0.38 ± 0.04	1.89 ± 0.06	4.3 ± 0.1	0.3 ± 0.1	2.52 ± 0.03	4.72 ± 0.08	0.6 ± 0.1
c_2	-0.79 ± 0.09	1.1 ± 0.1	-1.9 ± 0.2					-2.0 ± 0.5	-5.0 ± 0.6
c_3	1.28 ± 0.07	-1.8 ± 0.1	3.3 ± 0.1	-12.5 ± 0.2	-14.1 ± 0.4	-12.2 ± 0.5	-3.3 ± 0.2	-6.5 ± 0.4	-2.3 ± 0.5
c_4	-1.09 ± 0.05	-0.92 ± 0.08	-1.2 ± 0.1				-2.2 ± 0.1	-2.3 ± 0.2	-2.3 ± 0.3
c_5	-2.21 ± 0.04	-1.84 ± 0.06	-2.39 ± 0.08	-2.31 ± 0.05	-1.91 ± 0.09	-2.4 ± 0.1	-1.89 ± 0.05	-1.34 ± 0.08	-2.2 ± 0.1
c_6	0.45 ± 0.04	0.56 ± 0.06	0.39 ± 0.09						
c_7	-0.07 ± 0.01	-0.09 ± 0.02	-0.05 ± 0.03				2.2 ± 0.1		
c_8	0.74 ± 0.02	0.73 ± 0.03	0.82 ± 0.03						
c_9	0.61 ± 0.02	0.91 ± 0.04	0.51 ± 0.05						
χ^2			378	151	89	83	359	251	251
Degrees of freedom			374	140	94	90	311	248	239

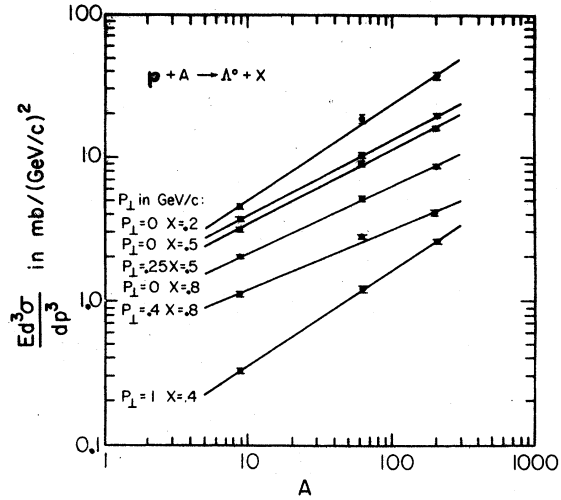


FIG. 17. Demonstration of the validity of the power-law A -dependence hypothesis for beryllium, copper, and lead data points at the same momentum and angle. The invariant cross sections for the "nucleon" were obtained by extrapolating these straight lines to $A = 1$.

terms of the variables (y, p_{\perp}^2) is plotted for the Be, Cu, and Pb Λ^0 spectra for $p_{\perp} = 0$ in Fig. 28. This is a reproduction of Fig. 4 in Ref. 9. Approximately half of the available forward rapidity was measured in this experiment. The decrease in differential multiplicity with increasing A is apparent in the figure. Figure 29, also reproduced from Ref. 9, shows a plot of the exponent $\alpha(x, p_{\perp})$ defined by Eq. (14), and Table VII gives these results in tabular form.

Figures 30 and 31 and Table VIII give the companion data for the K_S^0 spectra. The A dependence of the forward K_S^0 spectrum shape is qualitatively the same as that of the Λ^0 , but it is not so apparent in Fig. 30 because the region of phase space covered by the data is smaller. Thus the fixed cutoff at 60 GeV/c in laboratory momentum equals a larger center-of-mass rapidity for K_S^0 than for Λ^0 , and the maximum rapidity allowed is also correspondingly larger by about 0.8 units. Presumably, if the observed rapidity range were as large for K_S^0 as for Λ^0 , Fig. 30 would look more like Fig. 28. The exponent $\alpha(x, p_{\perp})$ contours for the smaller x values are smaller in magnitude for K_S^0 than for Λ^0 , perhaps an indication that rapidity (or velocity) is a better variable to use to compare the A dependence of spectra for different particles.

Figure 32 shows the α results for the $\bar{\Lambda}^0$ for completeness. The kinematic range is quite limited, but the results are in agreement with Fig. 29 for Λ^0 .

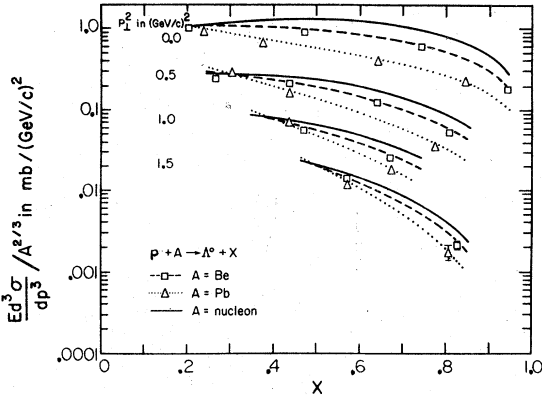


FIG. 18. Invariant cross sections for Λ^0/Σ production versus x with p_{\perp}^2 as a parameter. The cross sections have been scaled by $A^{-2/3}$ to plot beryllium, lead, and "nucleon" on the same graph. Some data points are shown for beryllium and lead. The smooth curves are the fits in Table VI.

C. Comparison with other experiments

Most published data on inclusive production of neutral strange particles by protons come from measurements in liquid-hydrogen bubble chambers. Experiments have been done in the 20-GeV range,^{25,26} at 100 GeV,²⁶ at 205 GeV,²⁷ and at 300 GeV.¹⁷ Since the measurements reported here were performed at 300 GeV with complex nuclear targets, some assumption regarding A dependence must be made to compare results. In addition, this experiment, with a 5-m-long dead space between production and detection, favors the projectile fragmentation region, while the more ac-

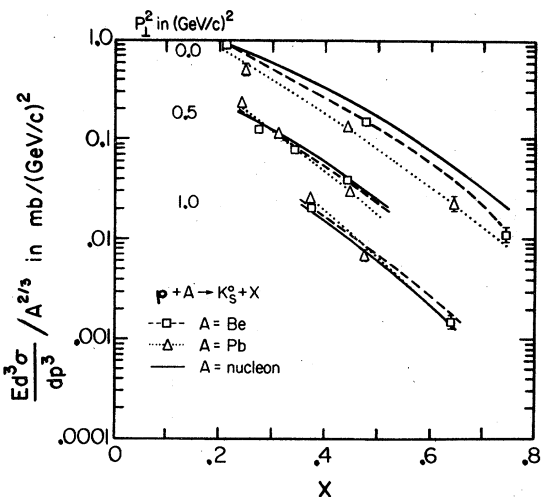


FIG. 19. Invariant cross sections for K_S^0 production divided by $A^{2/3}$ versus x with p_{\perp}^2 as a parameter.

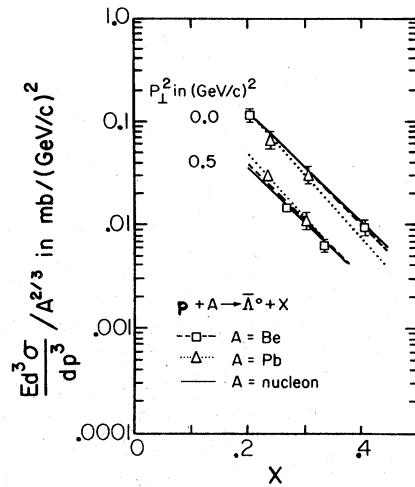


FIG. 20. Invariant cross sections for Λ^0 production divided by $A^{2/3}$ versus x with p_{\perp}^2 as a parameter.

curate bubble-chamber data are nearer the central region $|x| < 0.5$. Another difference between techniques is due to the solid angle accepted. In a bubble chamber a very large solid angle, or range in p_{\perp} , is viewed, but the overall statistics are limited. So it is often convenient to present the data as an invariant cross section integrated over all transverse momenta, rather than in the differential form $Ed^3\sigma/dp^3$. Here various fixed production angles were measured one at a time with good statistical accuracy. Some functional form for the invariant cross section must be assumed, however, to interpolate between the points and integrate overall p_{\perp} .

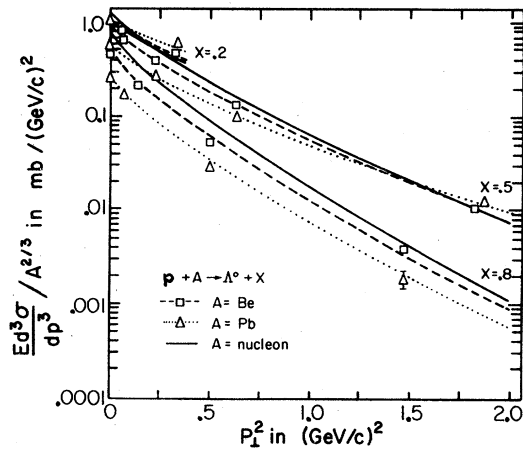


FIG. 21. Invariant cross sections divided by $A^{2/3}$ for Λ^0/Σ production versus p_{\perp}^2 with x as a parameter. Note the similarity in p_{\perp}^2 dependence shown by Figs. 21–23. The solid lines are from the fits given in Table VI.

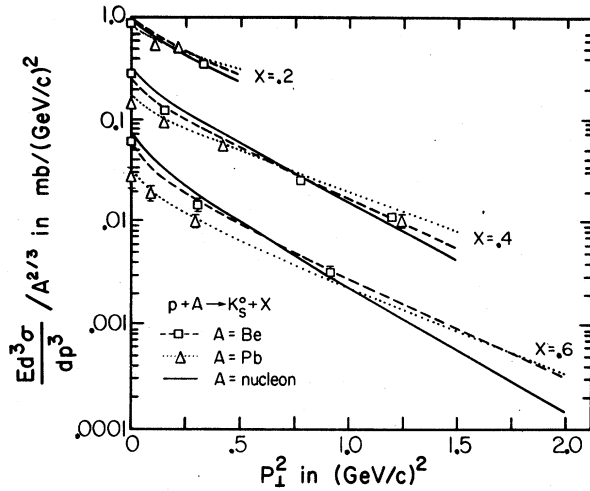


FIG. 22. Invariant cross sections divided by $A^{2/3}$ for K_S^0 production versus p_{\perp}^2 with x as a parameter.

In order to compare results from the two techniques, the extrapolated nucleon functional forms given in Table VI and discussed in Sec. IVA were integrated over all transverse momenta. Since it is impossible without accurate hydrogen data over the same phase-space region to test the hypothesis of extrapolation via Eq. (14), the error associated with this procedure cannot be accurately assessed. The results together with bubble-chamber data at several energies are shown in Fig. 33 for Λ^0 , Fig. 34 for K_S^0 , and Fig. 35 for $\bar{\Lambda}^0$. The shading on the figures represents only the uncertainties in the measured cross sections in this experiment. It is seen from the figures that the agreement for Λ^0 and K_S^0 is only qualitative. The comparison suffers from being sensitive to different regions of $|x|$ as discussed above. The Λ^0 spectrum does not show any peaking around $|x|=0.7$ as might be

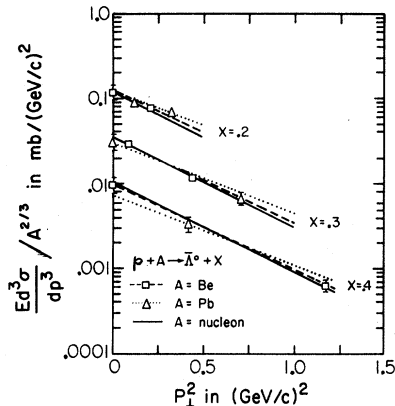


FIG. 23. Invariant cross sections divided by $A^{2/3}$ for Λ^0 production versus p_{\perp}^2 with x as a parameter.

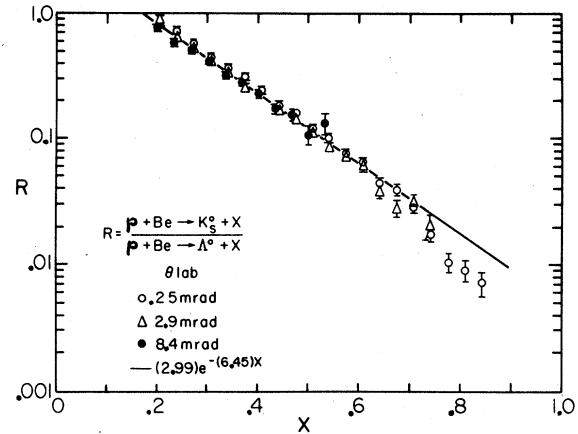


FIG. 24. The ratio of K_S^0 production to Λ^0 production for beryllium plotted versus x for various laboratory angles. The insensitivity of the ratio to production angle confirms the similarity of the two cross sections as a function of p_{\perp} . The line is intended to aid in comparing this figure with Fig. 25.

indicated by the 300-GeV spectrum of Ref. 17. There are very few $\bar{\Lambda}^0$ events, but it is clear from Fig. 35 that the cross section for $\bar{\Lambda}^0$ production has not become independent of energy at 24 GeV.

A graph showing inclusive production spectra in pp collisions at $p_{\perp} = 0.4$ GeV/c for a wide range of energies ($\sqrt{s} = 6.8$ GeV to $\sqrt{s} = 53$ GeV) is presented in Ref. 11. The higher-energy data come from the work of Antinucci *et al.*²⁸ The spectra are plotted as a function of laboratory rapidity $y_{\text{lab}} = y_{\text{max}} - y$, which reverses the shape of the curves shown, for example, in Fig. 28. Although neutral

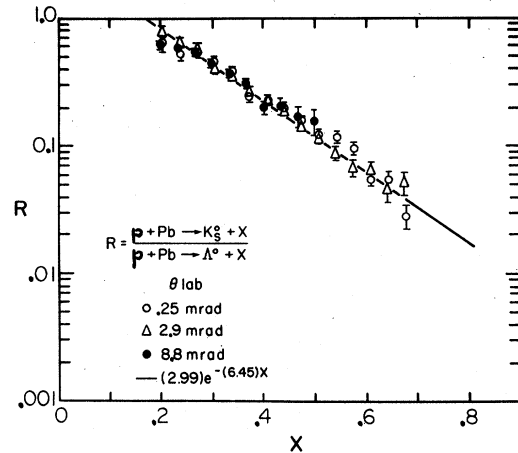


FIG. 25. The ratio of K_S^0 production to Λ^0 production, as in Fig. 24, but for lead. The ratio is again insensitive to angle, or p_{\perp} , and does not depend strongly on target nucleus.

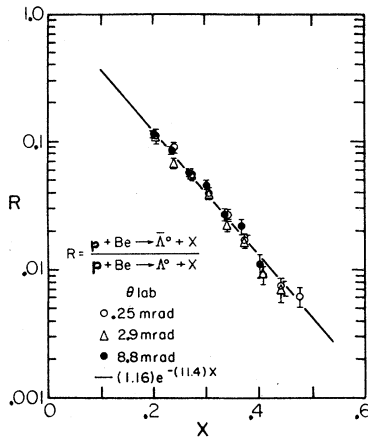


FIG. 26. The ratio of $\bar{\Lambda}^0$ production to Λ^0 production for beryllium plotted versus x for various laboratory angles. Again the ratio is independent of p_{\perp} . The solid line is intended to aid in comparing Figs. 26 and 27. Note that this line extrapolates to $\bar{\Lambda}^0/\Lambda^0 = 1$ at $x = 0$.

strange particle spectra are not given, inclusive cross sections for $pp \rightarrow \pi^+$, $pp \rightarrow \pi^-$, $pp \rightarrow K^+$, $pp \rightarrow K^-$, $pp \rightarrow p$, $pp \rightarrow \bar{p}$ are presented. In order to make a comparison with the present experiment, the spectra for $pp \rightarrow p$, $pp \rightarrow \bar{p}$, and $\frac{1}{2}[(pp \rightarrow K^+) + (pp \rightarrow K^-)]$ are replotted in Fig. 36, together with the extrapolated nucleon fits of Table VI evaluated at $p_{\perp} = 0.4$ GeV/c. The agreement between the \bar{p} and $\bar{\Lambda}^0$ spectra is remarkably good. The K_S^0 spectrum has the same shape as $\frac{1}{2}(K^+ + K^-)$, but is about 30% low. The Λ^0 spectrum is similar in

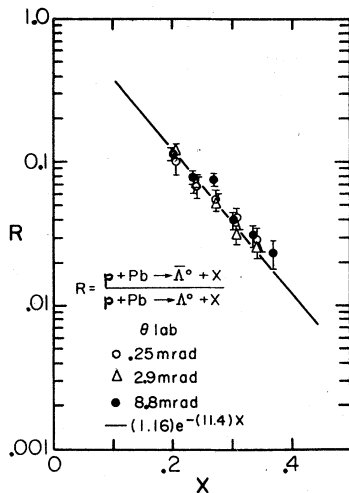


FIG. 27. The ratio of $\bar{\Lambda}^0$ production to Λ^0 production, as in Fig. 26, but for lead.

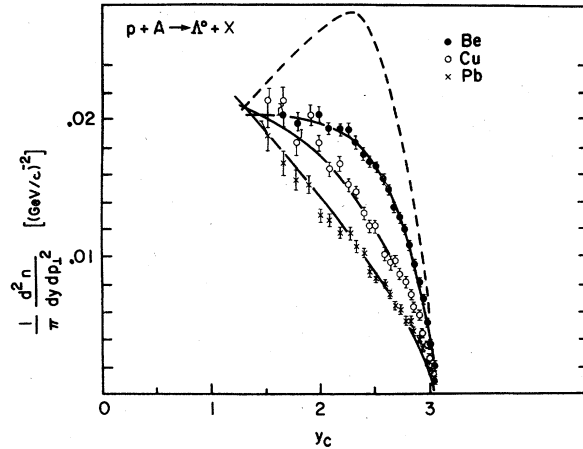


FIG. 28. The forward-direction invariant cross sections for Λ^0 production divided by the appropriate absorption cross section and plotted versus nucleon-nucleon center-of-mass rapidity. The dotted curve is the $A=1$ extrapolation. This plot is reproduced from Heller *et al.* (Ref. 9).

shape to the proton spectrum for $y_{\text{lab}} > 0.5$, but is about a factor of 10 smaller in magnitude.

D. Polarization of Λ^0 and $\bar{\Lambda}^0$

The inclusive Λ^0 data from beryllium, from which the cross sections in Table III were derived, were analyzed for Λ^0 polarization by exploiting the decay asymmetry in $\Lambda^0 \rightarrow p\pi^-$. The results of this analysis are discussed in detail in Ref. 7, where the first report was made of a substantial polarization effect in a high-energy inclusive reaction. A

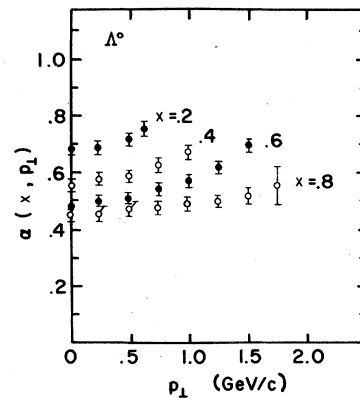


FIG. 29. The exponent $\alpha(x, p_{\perp})$ in the A dependence of the cross section for Λ^0 production as a function of p_{\perp} for various values of x . This graph is also reproduced from Ref. 9. The data are given in Table VII.

TABLE VII. Power-law hypothesis, $E \frac{d^3\sigma}{dp^3}(A) = A^{\alpha(x,p)} E \frac{d^3\sigma}{dp^3}(A=1)$.

$p + A \rightarrow \Lambda^0 + X^a$				
p_{\perp} (GeV/c)	$x=0.2$	$x=0.4$	$x=0.6$	$x=0.8$
0	0.676 ± 0.014	0.553 ± 0.014	0.480 ± 0.014	0.456 ± 0.014
0.25	0.685 ± 0.014	0.563 ± 0.014	0.490 ± 0.014	0.465 ± 0.014
0.50	0.708 ± 0.014	0.584 ± 0.014	0.506 ± 0.014	0.471 ± 0.014
0.75	0.748 ± 0.014	0.619 ± 0.014	0.532 ± 0.014	0.479 ± 0.014
1.00		0.673 ± 0.014	0.571 ± 0.014	0.492 ± 0.016
1.25			0.625 ± 0.015	0.511 ± 0.020
1.50			0.685 ± 0.020	0.528 ± 0.028
1.75				0.520 ± 0.070

$p + A \rightarrow K_S^0 + X$			$p + A \rightarrow \bar{\Lambda}^0 + X$		
p_{\perp} (GeV/c)	$x=0.2$	$x=0.4$	$x=0.6$	$x=0.2$	$x=0.4$
0	0.610 ± 0.016	0.546 ± 0.015	0.483 ± 0.018	0.67 ± 0.02	0.57 ± 0.02
0.25	0.625 ± 0.016	0.562 ± 0.014	0.500 ± 0.016	0.68 ± 0.02	0.58 ± 0.02
0.50	0.622 ± 0.016	0.596 ± 0.015	0.526 ± 0.017	0.70 ± 0.02	0.60 ± 0.02
0.75	0.722 ± 0.018	0.645 ± 0.015	0.560 ± 0.019	0.74 ± 0.02	0.64 ± 0.02
1.00	0.804 ± 0.024	0.712 ± 0.016	0.602 ± 0.021	0.80 ± 0.04	0.70 ± 0.03
1.25		0.794 ± 0.023	0.653 ± 0.027		0.77 ± 0.05
1.50			0.713 ± 0.03		

^a Taken from Ref. 9.

similar effect was subsequently observed in $p + \text{platinum} \rightarrow \Lambda^0 + X$ at 24 GeV.²⁹ As explained in Ref. 7, the Λ^0 spin direction was measured after precession in the magnetic field of the collimator, M2 in Fig. 2, resulting in two nonzero components, one longitudinal, i.e., along the Λ^0 line of flight,

and the other transverse and normal to the production plane. These two components were added quadratically to give a total polarization vector along the direction $(\vec{p}_{\Lambda} \times \vec{p}_p) / |\vec{p}_{\Lambda} \times \vec{p}_p|$ in Ref. 7. It was asserted in that report that the polarization was not a function of Feynman x , so all x 's were

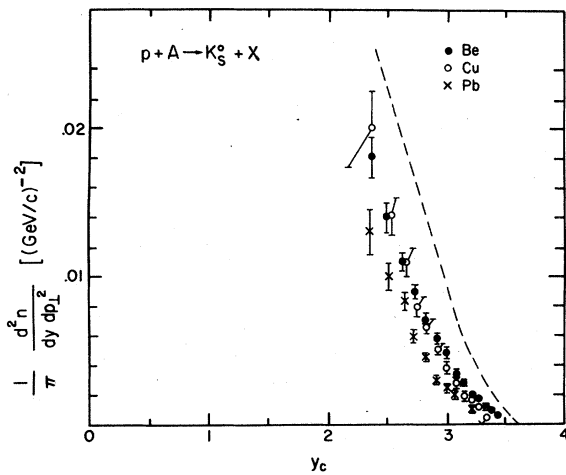


FIG. 30. Companion graph to Fig. 28 for the A dependence of the forward differential multiplicity for K_S^0 production. The dashed line represents the nucleon extrapolation.

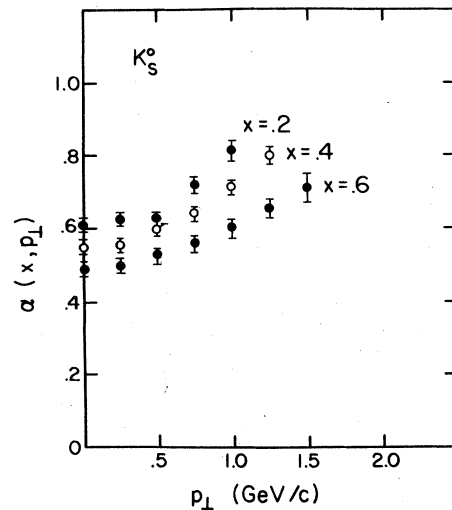


FIG. 31. The exponent $\alpha(x, p_{\perp})$ in the A dependence of the cross section for K_S^0 production as a function of p_{\perp} for various values of x . The data are given in Table VII.

TABLE VIII. Λ^0 polarization results for the reaction $p + \text{Be} \rightarrow \Lambda^0 + X$ at 300 GeV.
 $\hat{n} = (\vec{p}_p \times \vec{p}_\Lambda) / |\vec{p}_p \times \vec{p}_\Lambda|$.

Averaged over Feynman x		
p_\perp (GeV/c)	$\langle x \rangle$	$\vec{p} \cdot \hat{n}$
0.05	0.70	-0.013 ± 0.013
0.17	0.59	$+0.018 \pm 0.010$
0.25	0.73	-0.006 ± 0.011
0.39	0.65	-0.018 ± 0.012
0.59	0.55	-0.040 ± 0.013
0.78	0.48	-0.045 ± 0.012
0.99	0.53	-0.129 ± 0.015
1.18	0.54	-0.137 ± 0.021
1.39	0.58	-0.219 ± 0.039
1.55	0.58	-0.248 ± 0.078

For various values of Feynman x					
p_\perp (GeV/c)	x	$\vec{p} \cdot \hat{n}$	p_\perp (GeV/c)	x	$\vec{p} \cdot \hat{n}$
0.03	0.36	-0.10 ± 0.08	0.04	0.51	-0.022 ± 0.026
0.15	0.36	$+0.10 \pm 0.05$	0.16	0.51	$+0.020 \pm 0.015$
0.35	0.36	-0.14 ± 0.06	0.27	0.51	-0.016 ± 0.021
0.58	0.37	$+0.00 \pm 0.02$	0.44	0.47	$+0.017 \pm 0.021$
0.81	0.35	$+0.00 \pm 0.03$	0.52	0.56	-0.05 ± 0.026
1.05	0.38	-0.15 ± 0.03	0.76	0.49	-0.036 ± 0.018
			0.95	0.51	-0.11 ± 0.02
			1.18	0.51	-0.14 ± 0.02
			1.39	0.52	-0.14 ± 0.05
			1.55	0.58	-0.25 ± 0.08
0.05	0.69	-0.042 ± 0.022	0.07	0.88	$+0.37 \pm 0.026$
0.17	0.69	-0.013 ± 0.019	0.20	0.83	-0.019 ± 0.037
0.24	0.69	-0.001 ± 0.020	0.26	0.89	$+0.014 \pm 0.019$
0.34	0.69	-0.022 ± 0.019	0.40	0.88	-0.032 ± 0.026
0.62	0.68	-0.058 ± 0.018	0.75	0.86	-0.14 ± 0.03
1.03	0.68	-0.16 ± 0.03			
1.11	0.79	-0.16 ± 0.09			
1.40	0.67	-0.32 ± 0.06			

combined to give a plot of P_Λ vs p_\perp .

The same data are reproduced in Fig. 37(a) and 37(b), but the treatment of the two measured components of the polarization differs somewhat, and the polarization for various x values is shown to give the statistical validity of the claim made earlier that the polarization is x independent. To begin with, the sign convention has been reversed to conform to common usage in elastic scattering, namely positive polarization lies along $\hat{n} = (\vec{p}_p \times \vec{p}_\Lambda) / |\vec{p}_p \times \vec{p}_\Lambda|$. Then, to calculate the polarization vector at the production target, the average precession angle in the collimator magnet 122⁰⁷ was used to rotate the observed arrow backwards. This rotated polarization vector was then projected on the direction \hat{n} . The data in Fig. 37(a) are simply the points in Fig. 37(b) summed over

x . The statistical accuracy of the low- x data is poor, and there are no data at high x and high p_\perp , so the range over which the x independence is tested is about $0.5 \leq x \leq 0.8$. Table VIII gives the numbers. Very early data obtained from a copper target are consistent with the beryllium points and are also shown in Fig. 37(a).

The Λ^0 data samples used for the cross section and polarization analyses were substantially the same. In particular, the treatment of mass ambiguity between $\Lambda^0 \rightarrow p\pi^-$ and $K_s^0 \rightarrow \pi^+\pi^-$ discussed in Sec. III A above was followed in selecting the Λ^0 's for the polarization study. It was found that the very small K_s^0 contamination had a negligible effect on the Λ^0 decay asymmetry. A different approach was used to select $\bar{\Lambda}^0$'s for polarization study, however. In this case the algorithm used

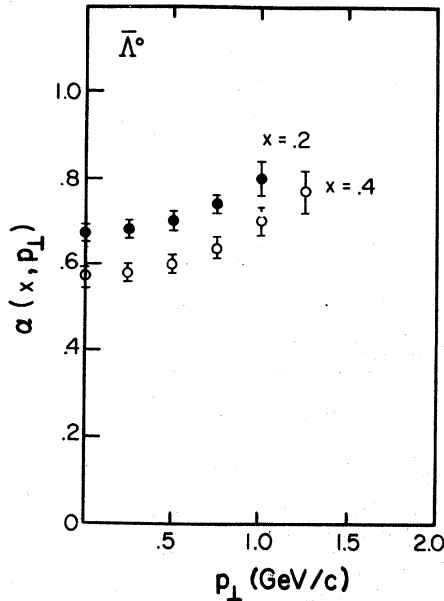


FIG. 32. The exponent $\alpha(x, p_{\perp})$ in the A dependence of the cross section for $\bar{\Lambda}^0$ production as a function of p_{\perp} for various values of x . The data are given in Table VII.

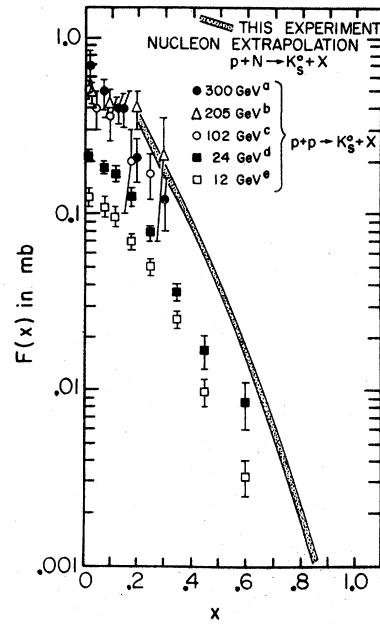


FIG. 34. Comparison of the integrated distribution $F(x)$ for K_s^0 production at various energies to the extrapolated nucleon distribution from this experiment. The function $F(x)$ is defined in the caption to Fig. 33, and the references are given there.

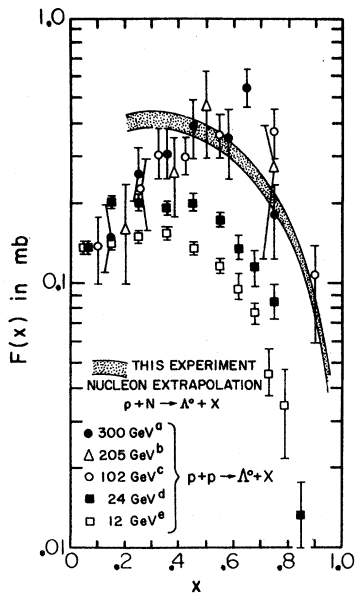


FIG. 33. The integrated distribution

$$F(x) = \frac{2}{\pi\sqrt{s}} \int E \frac{d^2\sigma}{dx dp_{\perp}^2} dp_{\perp}^2$$

for various hydrogen bubble-chamber experiments as a function of x compared to the extrapolated nucleon cross section of this experiment integrated over p_{\perp}^2 . The shading indicates the uncertainty in the nucleon extrapolation. The references for the bubble-chamber data are: (a) Sheng *et al.*, Ref. 17; (b) Charlton *et al.* (Ref. 27); (c) Chapman *et al.*, Ref. 26; (d) and (e) Blobel *et al.* (Ref. 25).

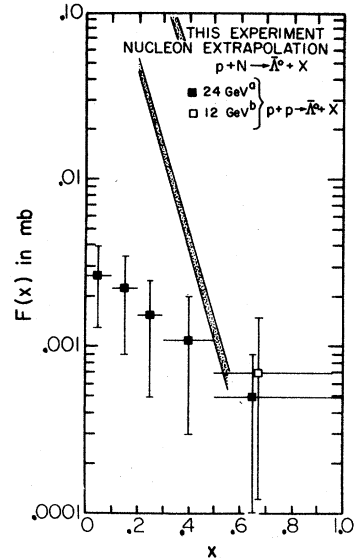


FIG. 35. Comparison of the integrated distribution $F(x)$ for $\bar{\Lambda}$ production given in Ref. 25 to the extrapolated nucleon distribution in this experiment. The function is defined in the caption to Fig. 33. It is clear that the $\bar{\Lambda}^0$ cross sections increase with energy between 24 and 300 GeV.

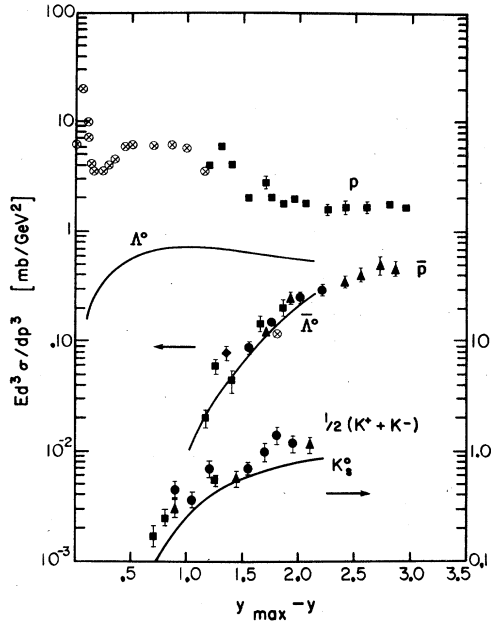


FIG. 36. Invariant cross sections for $p+p \rightarrow p+X$, $p+p \rightarrow \bar{p}+X$, and $\frac{1}{2}[(p+p \rightarrow K^+ + X) + (p+p \rightarrow K^- + X)]$ at $p_{\perp} = 0.4$ GeV/c versus $y_{\text{lab}} = y_{\text{max}} - y$ compared to the nucleon extrapolation results at the same p_{\perp} for $p+N \rightarrow \Lambda^0 + X$, $p+N \rightarrow \bar{\Lambda}^0 + X$, and $p+N \rightarrow K_S^0 + X$ from this experiment. The data points come from the work of Antinucci *et al.* (Ref. 28), and cover a range of equivalent bombarding energies from 270 to 1500 GeV. The Λ and \bar{p} results are similar in shape except near $y = y_{\text{max}}$, showing the leading particle nature of the hyperon cross section. The $\bar{\Lambda}^0$ and \bar{p} cross sections are remarkably similar. The K_S^0 cross section is about 30% below $\frac{1}{2}(K^+ + K^-)$, but has the same shape.

for the cross section, namely that all events simultaneously satisfying the $\bar{\Lambda}^0$ and K_S^0 mass hypotheses were rejected, was found too restrictive, and the helium gas Cherenkov counter was used to resolve the ambiguity and identify $\bar{\Lambda}^0 \rightarrow \bar{p}\pi^+$ for negative momenta in the range $50 \text{ GeV}/c \leq p \leq 160 \text{ GeV}/c$. Very few $\bar{\Lambda}^0$'s had momenta above 160 GeV/c. The component asymmetry analysis program was identical to the one used for the Λ^0 's. To obtain a $\bar{\Lambda}^0$ polarization vector at the beryllium target, it was assumed that the asymmetry parameter $\alpha_{\bar{\Lambda}} = -\alpha_{\Lambda}$,³⁰ and the magnetic moment $\mu_{\bar{\Lambda}} = -\mu_{\Lambda}$.³¹ The results are shown in Fig. 38. Although the statistical precision of the $\bar{\Lambda}^0$ data is not very good, there is no evidence that the Λ^0 and $\bar{\Lambda}^0$ polarizations are the same. For comparison, the $\bar{\Lambda}^0$ point at $p_{\perp} = 0.7$ GeV/c, $p_{\bar{\Lambda}} = -0.007 \pm 0.054$, is about 1 standard deviation away from the corresponding value of $p_{\Lambda} = -0.045 \pm 0.012$.

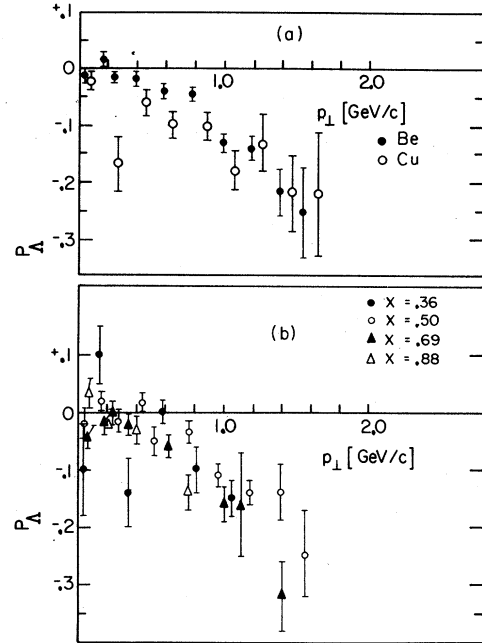


FIG. 37. Λ^0 polarization data. The solid circles have been previously shown in Ref. 7 with the opposite sign convention. The convention chosen here is that positive polarization is along $\hat{n} = (\vec{p}_p \times \vec{p}_{\Lambda}) / |\vec{p}_p \times \vec{p}_{\Lambda}|$. Early data taken with copper are also shown in Fig. 37(a) to give some indication of a lack of A dependence. The data from beryllium are divided up into various x bins in Fig. 37(b) to show the statistical validity of the x independence of the polarization. The beryllium numbers are given in Table VIII.

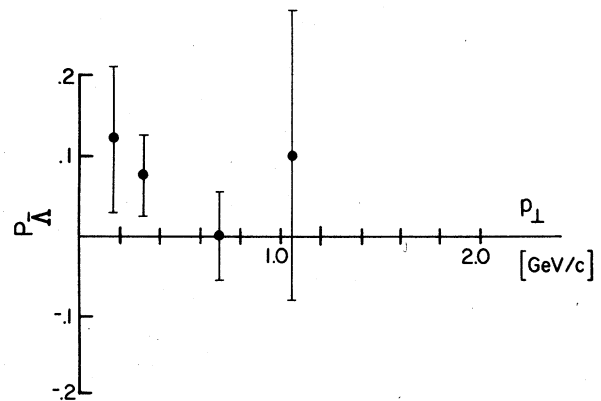


FIG. 38. Results of a search for $\bar{\Lambda}^0$ polarization. There is no evidence that the $\bar{\Lambda}^0$'s are polarized in a manner similar to the Λ^0 's.

TABLE IX. Evaluation of Eq. (A1) and comparison with data.

	N	C	A	B	$E \frac{d^3\sigma}{dp^3}$ (mb/GeV ²)	Data tables $Ed^3\sigma/dp^3$ (mb/GeV ²)
Λ^0	1550	1.27	0.28	0.642	3.70 ± 0.14	3.89 ± 0.08
K_s^0	129	1.22	0.13	0.688	0.60 ± 0.05	0.61 ± 0.03
$\bar{\Lambda}^0$	8	1.26	0.23	0.642	0.023 ± 0.007	0.024 ± 0.004

V. SUMMARY

A complete account of the inclusive measurements made at 300 GeV in the Fermilab neutral-hyperon beam has been given. The data are all presented in tabular form to facilitate their use by others. Three complex nuclear targets were used for the spectrum measurements, and the data were extrapolated to $A=1$ using a power law hypothesis for the A dependence. The extrapolated "nucleon" cross sections obtained in this manner have been compared to cross sections obtained by other experiments in pp collisions at various energies. From these comparisons it can be tentatively concluded that the Λ^0 cross section in the projectile fragmentation region essentially satisfies the scaling hypothesis by 100-GeV bombarding energy, that the K_s^0 cross section is perhaps still rising, that strange particle production remains about 10% of the cross section for the production of ordinary particles at 300 GeV, and that the cross sections for $\bar{\Lambda}^0$ at 300 GeV and \bar{p} up to 1000 GeV are quite comparable. In the quark model this last observation implies that the mechanism for producing antiquarks (presumably in quark-antiquark pairs) does so for \bar{s} and \bar{u} quarks with approximately equal strength.

The complete results of the search for Λ^0 and $\bar{\Lambda}^0$ polarization in inclusive production have been presented. The polarization of the Λ^0 's—about 20% at $p_{\perp} = 1.46$ GeV/ c —remains an intriguing and unexplained feature of inclusive production phenomena. Many properties of inclusive production seem to be dependent only on the broadest features of the strong interaction, and are insensitive to detail. The polarization phenomenon seems counter to this view, however, for coherence between amplitudes is required to obtain it. In the SU_6 quark model the spin of the Λ^0 is that of the strange quark. This feature might permit the use of Λ^0 polarization as a probe of quark dynamics.³²

ACKNOWLEDGMENTS

These measurements could not have been performed without the help of many people. Peter Koehler, C. N. Brown, Herman Haggerty, and the staff of the Meson Lab at Fermilab gave continued aid and support. The cryogenic group of R. Fast built and operated the superconducting magnet $M3$. R. McCracken helped construct the sweeping magnet $M2$. Much of the apparatus was built by G. Ott and E. Behr. This research was supported in part by the Department of Energy and in part by the National Science Foundation.

APPENDIX

This is a sample calculation of the cross sections using the raw data in Fig. 8. The momentum bins are 10 GeV/ c wide. In the bin centered at 145 GeV/ c , $N_{\Lambda} = 1550$, $N_K = 129$, and $N_{\bar{\Lambda}} = 8$. In Eq. (12) for the ion chamber, the relevant numbers are gated IC volts = 74 and the fraction of beam on target $f = 0.85$. These numbers can be combined with the calibration constant Eq. (5) to give $I = 9 \times 10^8$ protons. The beryllium target had 18.9×10^{23} nuclei. The solid angle $\Delta\Omega$ is given by (6). Then Eqs. (11) and (13) can be combined to give

$$E \frac{d^3\sigma}{dp^3} = \frac{NC}{AB} \times 3.38 \times 10^{-4} \text{ mb/GeV}^2, \quad (\text{A1})$$

where N is the number of events in the bin, C is the correction factor, A is the Monte Carlo acceptance from Table II, and B is the appropriate branching ratio.²⁰ These numbers are given in Table IX, where Eq. (A1) is evaluated, and compared to the numbers for the whole data sample (which involves more than one run) appearing in Tables III–V. An error of $\pm 3\%$ is ascribed to C as discussed in Sec. III E. The overall scale error is not included.

- *Present address: Rutgers, The State University, Piscataway, New Jersey 08854.
- †Present address: Lawrence Berkeley Laboratory, Berkeley, CA 94720.
- ‡Present address: Brookhaven National Laboratory, Upton, NY 11973.
- §Present address: Argonne National Laboratory, Argonne, IL 60439.
- ¶Present address: Bell Laboratories, Holmdel, NJ.
- ||Present address: Ford Motor Company, Allen Park, MI 48101.
- ¹R. H. March, in *1969 Summer Study*, edited by A. Roberts (National Accelerator Laboratory, Batavia, Illinois), Vol. 1, p. 173.
- ²L. Geweniger *et al.*, Phys. Lett. **48B**, 487 (1974), and several earlier papers.
- ³Y. Fukushima *et al.*, Phys. Rev. Lett. **36**, 348 (1976).
- ⁴S. Gjesdal *et al.*, Phys. Lett. **40B**, 152 (1972).
- ⁵F. Dydak *et al.*, Nucl. Phys. **B118**, 1 (1977).
- ⁶K. Heller *et al.*, in *Particles and Fields—1975*, proceedings of the Meeting of the Division of Particles and Fields of the American Physical Society, Seattle, edited by H. J. Lubatti and P. M. Mockett (Univ. of Washington, Seattle, 1976), p. 344.
- ⁷G. Bunce *et al.*, Phys. Rev. Lett. **36**, 1113 (1976).
- ⁸T. Devlin *et al.*, Nucl. Phys. **B123**, 1 (1977).
- ⁹K. Heller *et al.*, Phys. Rev. D **16**, 2737 (1977).
- ¹⁰For a general review, see H. Boggild and T. Ferbel, Ann. Rev. Nucl. Sci. **24**, 451 (1974).
- ¹¹Inclusive production of charged particles is discussed by U. Amaldi *et al.*, Nucl. Phys. **B86**, 403 (1975).
- ¹²R. P. Feynman, in *High Energy Collisions*, Stony Brook, 1969, edited by C. N. Yang *et al.* (Gordon and Breach, New York, 1969), p. 237.
- ¹³J. Whitmore, Phys. Rep. **27C**, 187 (1976).
- ¹⁴V. Hungerbuhler *et al.*, Phys. Rev. D **1**, 1203 (1975).
- ¹⁵J. Badier *et al.*, Phys. Lett. **39B**, 414 (1972).
- ¹⁶H. Boggild *et al.*, Nucl. Phys. **B57**, 1 (1973).
- ¹⁷A. Sheng *et al.*, Phys. Rev. D **11**, 1733 (1975).
- ¹⁸See, for example, T. Eichten *et al.*, Nucl. Phys. **B44**, 333 (1972); and W. F. Baker *et al.*, Phys. Lett. **51B**, 303 (1974). The charged-hyperon data of Refs. 14 and 15 were also taken on complex nuclear targets.
- ¹⁹H. Haggerty *et al.*, Nucl. Instrum. Methods **115**, 157 (1974).
- ²⁰ $\tau_{K^0} = 0.893 \times 10^{-10}$ sec, an average obtained by the Particle Data Group, Rev. Mod. Phys. **48**, S1 (1976). The branching ratios were also obtained from this reference.
- ²¹ $\tau_{\Lambda^0} = 2.61 \times 10^{-10}$ sec, E. F. Clayton *et al.*, Nucl. Phys. **B95**, 130 (1975). $\tau_{\Lambda^0} = \tau_{\Lambda^+}$ was assumed.
- ²²J. W. Cronin *et al.*, Phys. Rev. D **11**, 3105 (1975).
- ²³The spectrum shapes can be expressed at $p_{\perp}=0$ as a power of $(1-x)$: $Ed^3\sigma/dp^3 = (1-x)^n$. This function fits the data only approximately, giving best values $n_{\Lambda^0} = 0.6$, $n_{K^0} = 3.5$, $n_{\Lambda^+} = 6.0$ for beryllium. These exponents are predicted by the constituent interchange model. See R. Blankenbecler and S. J. Brodsky, Phys. Rev. D **10**, 2973 (1974).
- ²⁴K. Gottfried, Phys. Rev. Lett. **32**, 957 (1974).
- ²⁵V. Blobel *et al.*, Nucl. Phys. **B69**, 454 (1974).
- ²⁶J. Chapman *et al.*, Phys. Lett. **47B**, 465 (1973).
- ²⁷G. Charlton *et al.*, Phys. Rev. Lett. **30**, 574 (1973).
- ²⁸M. Antinucci *et al.*, Lett. Nuovo Cimento **6**, 121 (1973).
- ²⁹K. Heller *et al.*, Phys. Lett. **68B**, 480 (1977).
- ³⁰This is valid for arbitrary final-state interactions if CP invariance holds. See T. D. Lee, in *Preludes in Theoretical Physics*, edited by A. de-Shalit, H. Feshbach, and L. Van Hove (North-Holland, Amsterdam, 1966), p. 5.
- ³¹This is valid if TCP invariance holds.
- ³²G. L. Kane and Y.-P. Yao, Nucl. Phys. **B137**, 313 (1978); K. Heller, University of Michigan Report UMHE 77-38 (unpublished).